JGR Solid Earth

RESEARCH ARTICLE
10.1029/2024JB030041

A Recipe for Exotic Continental Fragment Formation: Key Constraints From Numerical Rift Models

Alan J. Yu[1,2], **Erkan Gün**[3,4], **Kenneth J. W. McCaffrey**[5], **and Philip J. Heron**[1,3]

[1]Department of Earth Sciences, University of Toronto, Toronto, ON, Canada, [2]Subsurface Process Modelling, GFZ Helmholtz Centre for Geosciences, Potsdam, Germany, [3]Department of Physical and Environmental Sciences, University of Toronto Scarborough, Toronto, ON, Canada, [4]MARUM—Center for Marine Environmental Sciences, University of Bremen, Bremen, Germany, [5]Department of Earth Sciences, Durham University, Durham, UK

Key Points:

- Structural inheritance from past Wilson Cycle(s) can facilitate continental fragment formation
- Inherited structure geometry directly controls fragment width, while the geotherm influences rift style (wide vs. narrow)
- Modeled fragments reproduce dimensions consistent with many geological examples

Correspondence to:

A. J. Yu,
alan.yu@gfz.de

Citation:

Yu, A. J., Gün, E., McCaffrey, K. J. W., & Heron, P. J. (2025). A recipe for exotic continental fragment formation: Key constraints from numerical rift models. *Journal of Geophysical Research: Solid Earth*, *130*, e2024JB030041. https://doi.org/10.1029/2024JB030041

Received 30 JUL 2024
Accepted 19 SEP 2025

Author Contributions:

Conceptualization: Alan J. Yu, Philip J. Heron
Data curation: Alan J. Yu
Formal analysis: Alan J. Yu, Philip J. Heron
Funding acquisition: Philip J. Heron
Investigation: Alan J. Yu, Philip J. Heron
Methodology: Alan J. Yu, Philip J. Heron
Project administration: Philip J. Heron
Resources: Alan J. Yu, Philip J. Heron
Software: Alan J. Yu, Philip J. Heron
Supervision: Philip J. Heron
Validation: Alan J. Yu, Philip J. Heron
Visualization: Alan J. Yu, Erkan Gün, Philip J. Heron
Writing – original draft: Alan J. Yu, Erkan Gün, Kenneth J. W. McCaffrey, Philip J. Heron
Writing – review & editing: Alan J. Yu, Erkan Gün, Kenneth J. W. McCaffrey, Philip J. Heron

Abstract The Wilson Cycle describes the opening and closing of oceans, generating new plate boundaries at continental rifts, and extinguishing ancient plate boundaries with continental collisions (creating a continental suture). However, the general view of the Wilson Cycle does not fully explain more complex tectonic scenarios. For example, rifting can create exotic continental fragments, where a piece of continent becomes displaced from its principal part and stranded on another tectonic plate. Despite the prevalence of stranded fragments in the geological record, their formation processes remain poorly understood. Here, we conducted 2-D numerical rift models to systematically test the tectonic influence of a variety of inherited geological structures that could be generated from the closing of an old plate boundary. Through automated detection of continental breakup and measurement of continental fragment dimensions, the models show that fragment width is directly controlled by the geometry of the inherited structures, including the dip angle and extent of the old subduction suture, as well as the extent of orogenic deformation. However, the initial geotherm, strain and rheological weaknesses in both the crust and mantle lithosphere, along with the divergence rate, can influence strain localization during rifting. Notably, a very ductile lithosphere leads to prolonged delocalized thinning and wider rifts. Overall, the models produce continental fragments in widths ~175–350 km, aligning with many geological examples. Moreover, our work provides key physical constraints that can be applied in future regional applications and highlights the role of different forms of structural inheritance during rifting and continental fragment formation.

Plain Language Summary The opening of a new ocean can separate a continental fragment from its parent plate, adding complexity to our understanding of Earth's tectonic cycle. Despite a growing catalog of identified examples, the processes involved in their formation remain poorly understood. We use numerical models to simulate continental extension, incorporating various deformed structures inherited from ancient tectonic cycles to analyze their influence on fragment formation. Our models show that the width of the continental fragment is directly linked to the geometry of inherited structures, but the fragment formation process can also be influenced by the pre-existing temperature gradient, extension velocity, and weaknesses throughout the lithosphere. Agreeing with a number of real-world observations, our work provides a recipe for continental fragment formation that can be applied in future regional models.

1. Introduction

Continental fragments, also known as terranes or slivers, are small pieces of the Earth's lithosphere that have previously separated from a larger continental plate (Vink et al., 1984). They possess similar geological signatures to their parent continent (Myers, 1987; Tucker et al., 2001) and are often the products of successful rifting during the breakup of supercontinents (Tetreault & Buiter, 2014).

The presence of continental fragments is an added layer of complexity to the Wilson Cycle (Schiffer et al., 2019), which proposes a sequence where oceans open through continental extension (i.e., rifting) and later close due to subduction and continental collision (Wilson, 1966, 1969). Traditionally, the location of ocean margins is thought to be aligned with the remnant sutures of previous ocean closures (Dewey & Burke, 1974; Murphy et al., 2006; Wilson, 1966). While many examples of this phenomenon exists along the ancient orogenic belts (e.g., the Atlantic orogenies), there are instances where the breakup does not coincide with the marked location of the preceding suture (Buiter & Torsvik, 2014; Schiffer et al., 2020; Wilson, 1966). For example, the Northeast Atlantic Ocean, which separated Greenland and Eurasia, did not open near the suture of the previous Iapetus Ocean closure (Figure 1; Buiter & Torsvik, 2014). The continental lithosphere—particularly near its margins—is

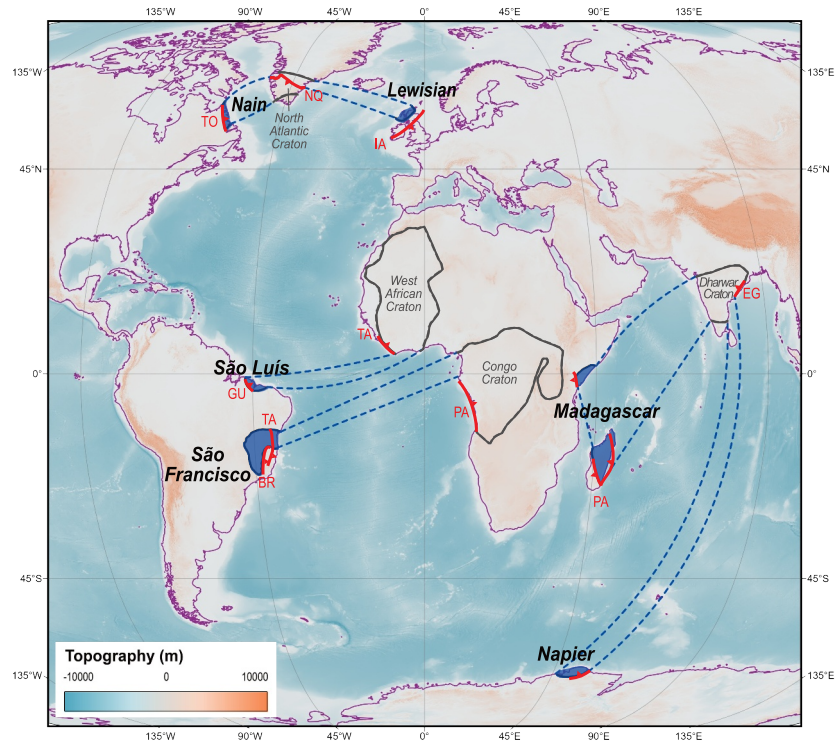

Figure 1. Geological examples of exotic continental fragments (blue), along with their parent continents (gray) and associated sutures (red). Detailed tectonic history is provided in the Discussion. Bedrock topography is obtained from the ETOPO 2022 Global Relief Model (NOAA National Centers for Environmental Information, 2022). Abbreviations: TO–Torngat Orogen (St-Onge et al., 2009; Wardle et al., 1990), NQ–Nagssugtoqidian Orogen (Kolb, 2014; Park, 2022), IA–Iapetus Suture (Buiter & Torsvik, 2014), GU–Gurupi Orogen (Klein et al., 2005; Klein & Moura, 2008), TA–Trans-Amazonian Orogen (Aguilar et al., 2017; Alkmim, 1998), BR–Brasiliano Orogen (Pedrosa-Soares, 2001), PA–Pan-African Orogen (De Wit et al., 2008; Fritz et al., 2013; Schofield et al., 2010), EG–Eastern Ghats Orogen (Boger et al., 2001; Collins & Pisarevsky, 2005).

highly deformable (Willingshofer et al., 2013), and identifying the breakup location involves more than simply tracing past sutures. Indeed, plate extension and breakup can leave behind a fragment of the parent continent, as seen with the Lewisian Complex in northwestern Scotland (Figure 1; Bridgwater et al., 1973).

Figure 2 outlines the process by which an exotic continental fragment could be generated through Wilson Cycles processes. During subduction, the accretion and subduction of terranes can introduce rheological heterogeneities in the overriding continent, at times extending up to a few hundred kilometers inland from the trench (Figure 2a; Mason & Brewer, 2004; Tetreault & Buiter, 2012). Melting above the subducting slab can introduce magmatic intrusions that significantly rework the overriding continental lithosphere (Figure 2a; Gerya & Meilick, 2011; Tatsumi, 1989). In addition, the overriding continental plate can produce prominent mountain ranges and associated volcanism, such as the Andes (Figure 2a; Cembrano & Lara, 2009; Pons et al., 2023).

The closure of an ocean basin and the ensuing collision of continents are known to produce long-lasting, lithospheric-scale deformation (Figure 2b; Schellart et al., 2019; Vauchez et al., 1997). The collision interface is typically marked by a narrow, highly deformed suture separating the two distinct geological domains (Figure 2b), such as the Indus Suture and the Bitlis-Zagros Suture (Dewey & Bird, 1970; Pysklywec et al., 2002). However, deformation can extend well beyond the collision interface; complex orogenic belts can arise, with deformation patterns shaped by pre-existing structures, lithology, and tectonic history (Figure 2b; Dewey, 1977).

The resulting suture zone may preserve extensive deformation from both types of Wilson Cycle events (Cawood et al., 2018; Schiffer et al., 2015; Thomas, 2019). Driven by the reactivation of lithospheric structures inherited from previous Wilson Cycle events (Figure 2c), an exotic continental fragment could be produced in subsequent continental extension (Figure 2d).

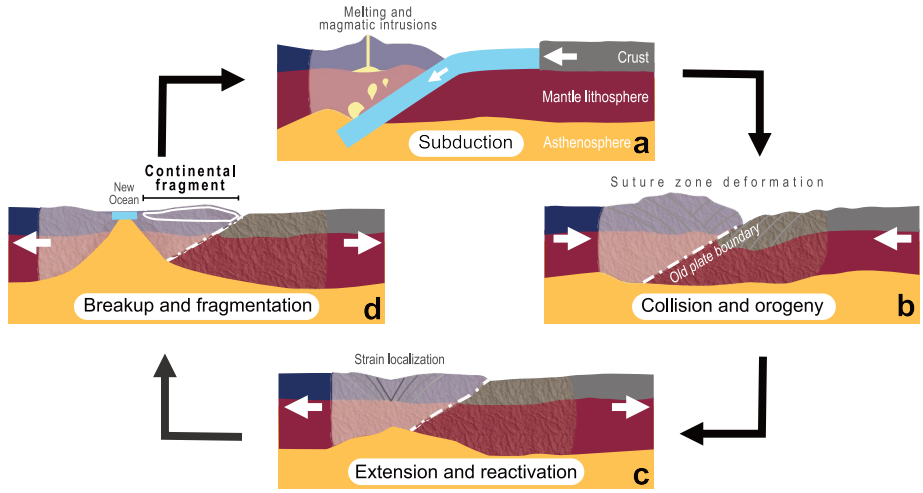

Figure 2. Proposed tectonic mechanism for the formation of a continental fragment. (a) At convergent boundaries, subduction produces pervasive deformation in the overriding continent. (b) Following ocean closure, the consequent continental collision can generate lithospheric-scale deformation preserved in both plate margins. (c) Structural inheritance from the previous subduction and collision may be reactivated during later extension, localizing strain away from the old plate boundary. (d) Upon successful breakup, such inheritance can isolate an exotic continental fragment stranded on the conjugate plate.

Using both analog (e.g., Beniest et al., 2018; Brun, 1999) and numerical models (e.g., Dubinin et al., 2018; Gueydan & Précigout, 2014; Heron et al., 2019), rifting and continental breakup have been extensively studied. Although factors controlling the style of rifted margins have been widely debated (e.g., Brune et al., 2014; Gouiza & Naliboff, 2021; Huismans & Beaumont, 2003), limited attention has been given to fragment formation (cf. Heron et al., 2023). This study addresses the gap by exploring the role of various forms of structural inheritance, implemented in previous rift studies, in controlling fragment formation. We identify and test a set of physical parameters governing the inherited structures and rift processes to analyze their influence on the generated fragment (see Methods). We then place the modeling work into context by comparing it with geological examples (see Discussions).

2. Methods

2.1. Governing Equations

In this study, we use the numerical code ASPECT (version 2.4.0-pre, commit 9da28e8) to solve equations for a highly viscous fluid driven by differences in density and temperature (Bangerth et al., 2022; Fraters et al., 2019; Heister et al., 2017; Kronbichler et al., 2012). We assume an incompressible medium with an infinite Prandtl number (i.e., the Boussinesq approximation). This approximation is widely used in lithospheric-scale simulations (e.g., Brune et al., 2014) and is valid so long as density variations are small, and the modeled processes do not induce significant shear or adiabatic heating (Gerya, 2019). With this approximation, the thermo-mechanical system is governed by the conservation of mass (Equation 1), linear momentum (Equation 2), and energy (Equation 3).

$$\nabla \cdot \mathbf{u} = 0 \tag{1}$$

$$-\nabla \cdot (2\eta \dot{\boldsymbol{\varepsilon}}) + \nabla P = \rho \mathbf{g} \tag{2}$$

$$\rho C_p \left(\frac{\partial T}{\partial t} + \mathbf{u} \cdot \nabla T \right) - \nabla \cdot k \nabla T = \rho H \tag{3}$$

where $\mathbf{u}$ is the velocity, η the viscosity, $\dot{\boldsymbol{\varepsilon}} = \frac{1}{2}\left(\nabla \mathbf{u} + (\nabla \mathbf{u})^T\right)$ the deviatoric strain rate tensor, P the pressure, ρ the density, $\mathbf{g}$ the gravitational acceleration, C_p the heat capacity, T the temperature, t the time, k the thermal

conductivity, and H the rate of internal heat production per unit volume (typically due to the radioactive decay of elements).

Compositional fields are used to track distinct material fields (e.g., upper crust, lower crust, mantle lithosphere, and asthenosphere) and other time-dependent quantities (e.g., plastic strain and viscous strain). The compositional fields are non-diffusive and advected with the flow, thus introducing an additional advection equation:

$$\frac{\partial c_i}{\partial t} + \mathbf{u} \cdot \nabla c_i = q_i \tag{4}$$

where c_i is the advected quantity of the compositional field, and q_i is the reaction rate (zero for all material fields and non-zero for accumulated strain fields).

To relate the material properties to the physical state, we employ an equation of state wherein density varies linearly:

$$\rho = \rho_0(1 - \alpha(T - T_0)) \tag{5}$$

where ρ is the density, ρ_0 the reference density, α the thermal expansivity, T the temperature, and T_0 the reference temperature.

2.2. Rheological Flow Laws

ASPECT can simulate strain localization and weakening processes in deforming rocks using rheological flow laws derived from laboratory experiments (Döhmann et al., 2019). All material fields are prescribed a visco-plastic rheology with a composite set of flow laws that simultaneously account for dislocation creep and diffusion creep (Glerum et al., 2018). The viscosity of rocks is calculated according to the following flow law:

$$\eta = \frac{1}{2} A^{-\frac{1}{n}} d^{\frac{m}{n}} \dot{\varepsilon}_{\mathrm{II}}^{\frac{1-n}{n}} \exp\left(\frac{Q^* + PV^*}{nRT}\right) \tag{6}$$

where A is the material constant, n the stress exponent, $\dot{\varepsilon}_{\mathrm{II}} = \sqrt{\frac{1}{2}\dot{\varepsilon}_{\mathrm{ij}}\dot{\varepsilon}_{\mathrm{ij}}}$ (strictly for incompressible medium) is the square root of the second invariant of the deviatoric strain rate, d the mineral grain size, m the grain size exponent, Q^* the reference activation energy, V^* the reference activation volume, P the pressure, R the ideal gas constant, and T the temperature. Moreover, the dislocation viscosity η_{disl} is grain size-independent ($n > 1, m = 0$), and the diffusion viscosity η_{diff} is strain rate-independent ($n = 1, m \neq 0$). These lead to Equations 7 and 8 for the dislocation and diffusion creep viscosity, respectively:

$$\eta_{\mathrm{disl}} = \frac{1}{2} A_{\mathrm{disl}}^{-\frac{1}{n}} \dot{\varepsilon}_{\mathrm{II}}^{\frac{1-n}{n}} \exp\left(\frac{Q^*_{\mathrm{disl}} + PV^*_{\mathrm{disl}}}{nRT}\right) \tag{7}$$

$$\eta_{\mathrm{diff}} = \frac{1}{2} A_{\mathrm{diff}}^{-1} d^m \exp\left(\frac{Q^*_{\mathrm{diff}} + PV^*_{\mathrm{diff}}}{RT}\right) \tag{8}$$

The effective viscosity in the ductile regime is restricted within a pre-defined minimum (10^{18} Pa s) and maximum value (10^{26} Pa s) and is calculated by

$$\eta_{\mathrm{eff,vi}} = \left(\frac{1}{\eta_{\mathrm{disl}}} + \frac{1}{\eta_{\mathrm{diff}}}\right)^{-1} \tag{9}$$

We introduce an additional rheological strength parameter f to Equations 7 and 8, which allows us to discretely scale the effective viscosity of a material field:

$$f = \frac{(A'_{\mathrm{disl\ |\ diff}})^{-\frac{1}{n}}}{(A_{\mathrm{disl\ |\ diff}})^{-\frac{1}{n}}} = \left(\frac{A_{\mathrm{disl\ |\ diff}}}{A'_{\mathrm{disl\ |\ diff}}}\right)^{\frac{1}{n}} \tag{10}$$

The adjusted material constant A' can thus be expressed as

$$A'_{\text{disl,diff}} = \frac{A_{\text{disl,diff}}}{f^n} \tag{11}$$

where A is the reference material constant for that field. When $f = 0.5$ is applied to a material field, the effective viscosity of that field becomes half of its unstrained value.

The total strain rate is the superposition of partial strain rates from both creep mechanisms (Gueydan & Précigout, 2014; Precigout et al., 2007):

$$\dot{\varepsilon}_{\text{total}} = \dot{\varepsilon}_{\text{disl}} + \dot{\varepsilon}_{\text{diff}} \tag{12}$$

where the corresponding strain rates are

$$\dot{\varepsilon}_{\text{disl}} = A_{\text{disl}} \exp\left(-\frac{Q^*_{\text{disl}} + PV^*_{\text{disl}}}{RT}\right)\sigma^n_{\text{II,disl}} \tag{13}$$

$$\dot{\varepsilon}_{\text{diff}} = A_{\text{diff}} \exp\left(-\frac{Q^*_{\text{diff}} + PV^*_{\text{diff}}}{RT}\right)\sigma_{\text{II,diff}} d^{-m} \tag{14}$$

where σ_{II} is the square root of the second invariant of the deviatoric stress. The strain rates determined by both creep mechanisms are sensitive to temperature and pressure, but the relative contribution between these creeps differs drastically under different conditions (Karato & Wu, 1993). The mechanism contributing to a higher strain rate becomes the dominant creep, which may exert a greater influence on deformation development. Equations 13 and 14 can also be rearranged to obtain the viscous yield stresses for both creep mechanisms at the start of the model run:

$$\sigma'_{\text{II,disl}} = \left(\frac{\dot{\varepsilon}'}{A_{\text{disl}}}\right)^{1/n} \exp\left(\frac{Q^*_{\text{disl}} + PV^*_{\text{disl}}}{nRT}\right) \tag{15}$$

$$\sigma'_{\text{II,diff}} = \left(\frac{\dot{\varepsilon}'}{A_{\text{diff}}}\right) \exp\left(\frac{Q^*_{\text{diff}} + PV^*_{\text{diff}}}{RT}\right) d^m \tag{16}$$

where $\dot{\varepsilon}'$ is the reference strain rate.

In the brittle part of the lithosphere, plasticity restricts stress through a Drucker-Prager yield criterion formulation. This criterion defines the plastic yield stress, the minimum stress at which a rock undergoes permanent plastic deformation. In two-dimensional (2-D) systems, the plastic yield stress is expressed by:

$$\sigma'_{\text{II,pl}} = C\cos\phi + P\sin\phi \tag{17}$$

where P is the pressure, C the cohesion, and ϕ the angle of internal friction. When viscous stress exceeds ($\sigma_{\text{II}} = 2\eta_{\text{eff,vi}}\dot{\varepsilon}_{\text{II}}$) the plastic yield stress, the effective viscosity is rescaled back to the yield surface:

$$\eta_{\text{eff,pl}} = \frac{\sigma'_{\text{II,pl}}}{2\dot{\varepsilon}_{\text{II}}} \tag{18}$$

2.3. Structural Inheritance

The continental lithosphere can be altered by various types of inherited structures (Cawood et al., 2018; Gouiza & Naliboff, 2021; Manatschal et al., 2015; Samsu et al., 2023): mechanical strain (faults, shear zones, folds), thermal anomalies (mantle upwelling, magma chambers), and rheological heterogeneities (magmatic arcs, mantle serpentinites, ophiolites, intrusions). These structures, varying in scale and depth throughout the lithosphere, may significantly control the deformation pattern upon reactivation (Beniest et al., 2018; Fossen et al., 2017; Heron et al., 2016a, 2016b, 2019; Petersen & Schiffer, 2016; Piqué & Laville, 1996).

Previous numerical models have implemented inherited structures in several ways. A common method involves prescribing a weak seed in the initial lithosphere (e.g., Huismans & Beaumont, 2003; Salazar-Mora et al., 2018). The seed effectively controls the focal point of deformation development. However, the placement of a weak seed does not offer insights into the role of the geometry of inherited structures.

Another method is by modifying the variables used to determine the viscosity and strain rate of the material field —notably the material constant A (e.g., Brune et al., 2014; Heron et al., 2016a, 2016b; Pysklywec et al., 2002). This approach can simulate large-scale discrete rheological variations, such as different crustal domains or a hydrated mantle.

Recently, an increasing number of studies have opted to prescribe a zone of white noise random initial strain to represent a diffused zone of varying degrees of smaller-scale deformation (e.g., Gouiza & Naliboff, 2021; Richter et al., 2021). Strain variation within the zone can be adjusted, enabling models to account for the uncertainty of heterogeneities arising from complex tectonic settings.

In this study, we combine the last two approaches by applying the strength parameter f (Equation 10) to one or more material fields, and by introducing a white noise pattern of initial plastic strain on both sides of the continental suture (using ASPECT's rand_seed function).

2.4. Model Setup

The 2-D models feature four layers of different rock composition (Figure 3a): a 20 km-thick upper crust composed of wet quartzite (Gleason & Tullis, 1995), a 20 km-thick lower crust of wet anorthite (Rybacki et al., 2006), an 80 km-thick mantle lithosphere of dry olivine (Hirth & Kohlstedt, 2003), and a 480 km-thick asthenosphere of wet olivine (Hirth & Kohlstedt, 2003). Each layer is compositionally homogeneous, and its material properties are listed in Table 1. The 2-D models are conducted in a 600 km (x-axis) by 600 km (z-axis) cross-section. High-resolution grids of 0.5 km are prescribed above 200 km depth, while a lower resolution of 2 km per grid is used below for computational efficiency.

The initial continental lithosphere is designed as an idealized pre-rift configuration that reflects the complex tectonic inheritance at the suture of two plates. We set up an upper plate and a lower plate with an angled old plate boundary between them (Figure 3a). The suture zone has two components: First, the upper plate margin is rheologically weakened by modifying the material constant using f (see Figure 3b). This represents discrete inherited structures unique to the overriding plate resulting from a potential previous subduction event (e.g., magmatic intrusions). Second, a deformation zone creates a region weakened by the initial plastic strain with a base value of 0.5 and a randomized range from 0.5 to 1.5 within the domain (see Figure 3c). This represents widespread deformation across both plate margins from earlier collision and orogeny.

As rocks undergo strain, they require less applied stress to further deformation—a phenomenon known as strain weakening (or material softening). In numerical models, this is shown by a reduction of brittle strength in faults or effective viscosity in ductile shear zones (e.g., Gueydan et al., 2014). Under plastic strain, the internal angle of friction and cohesion are linearly weakened from 30° to 15° and from 20 to 10 MPa, respectively, over the plastic strain interval of 0.5–1.5. Under viscous strain, the material constant is linearly weakened to half of the unstrained value over the viscous strain interval of 0.5–1.5.

An outward flow of $v = 5$ mm yr^{-1} is applied to the top 120 km of both model side boundaries (10 mm yr^{-1} in total), which is balanced by an area-equivalent inflow from the model's bottom boundary. The top boundary of the model is defined by a free surface, with a small amount of surface diffusion to account for erosion and deposition governed by:

$$\frac{\partial h}{\partial t} = \gamma \frac{\partial^2 h}{\partial x^2} \tag{19}$$

where h is the surface elevation, and $\gamma = 1 \times 10^{-7}$ m^2 s^{-1} is the surface diffusion coefficient (e.g., Ruh et al., 2022).

We implement the initial temperature profile of the model using the one-dimensional steady-state continental geotherm (Chapman, 1986):

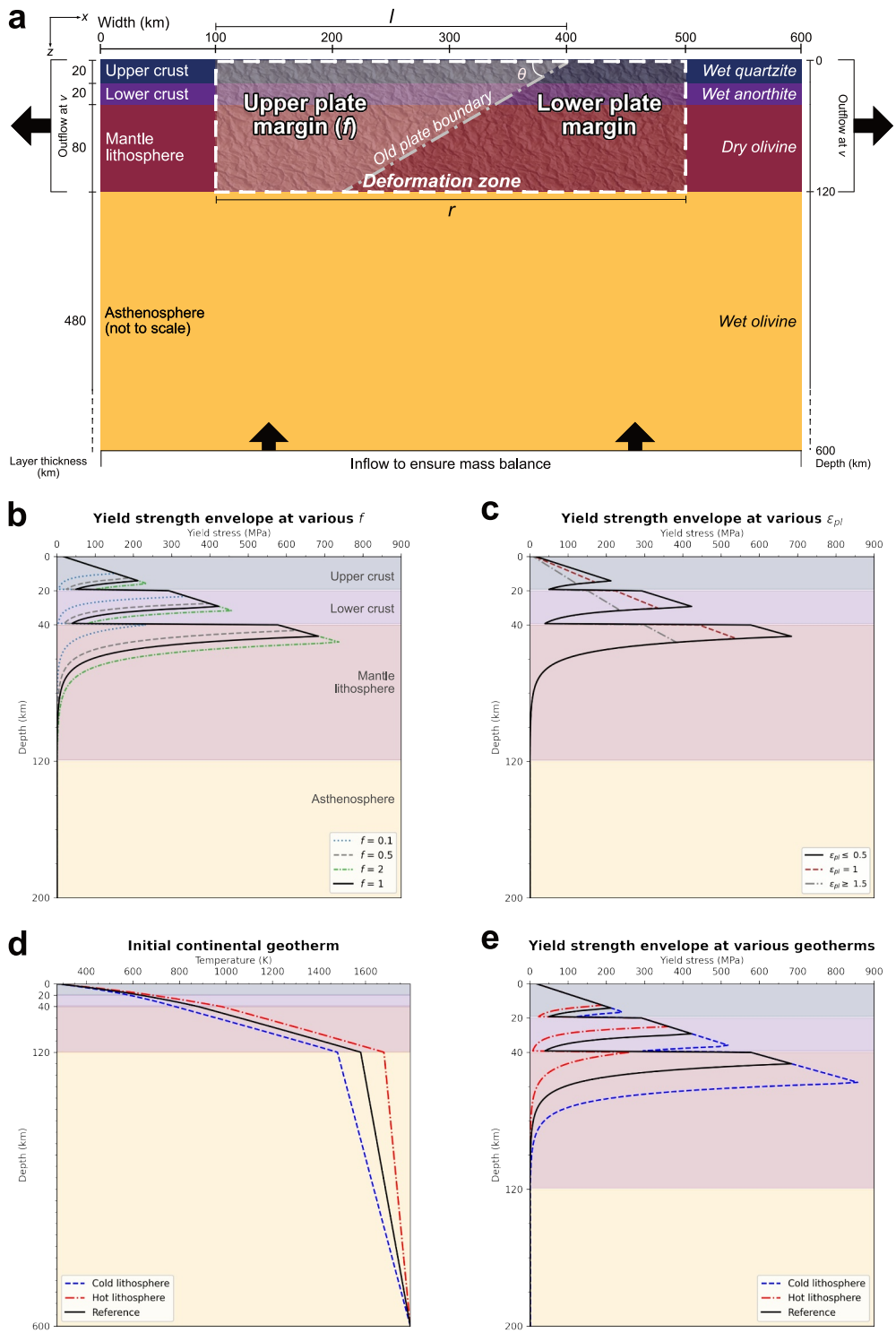

Figure 3. (a) Initial numerical setup of the rift models. The effective viscosity of the upper plate margin (shaded white) is modified by the strength parameter f. θ is the dip angle of the old plate boundary, l is the width of the weakened upper plate margin, r is the extent of the deformation zone, and v is the extension velocity. (b) Yield strength envelope of the initial continental lithosphere at various f values, obtained using Equations 15–17 and parameters from Table 1, assuming a reference strain rate of 10^{-15} s^{-1}. Note that when $f = 0.1$, the mantle lithosphere is completely ductile. (c) Yield strength envelope of the initial continental lithosphere at various plastic strain values due to strain weakening. (d) Initial temperature profile of the reference, cold, and hot lithosphere, obtained using Equations 20–22 and parameters from Table 2. (e) Yield strength envelope of the initial continental lithosphere at various initial geotherms.

Table 1
The Material Properties of the Four Model Layers

Material property	Units	Upper crust	Lower crust	Mantle lithosphere	Asthenosphere
Thickness (Δz)	m	20e3	20e3	80e3	480e3
Density (ρ)	kg m^{-3}	2,800	2,900	3,250	3,300
Thermal conductivity (k)	m^2 s^{-1}	2.5	2.5	3	3
Thermal expansivity (α)	K^{-1}	2.5e−5	2.5e−5	2.5e−5	2.5e−5
Internal heat production rate (H)	W m^{-3}	1e−6	4e−7	2e−8	0
Specific heat capacity (C_p)	J kg^{-1} K^{-1}	750	750	750	750
Rheology		Wet quartzite	Wet anorthite	Dry olivine	Wet olivine
Dislocation creep					
Material constant (A_{disl})	Pa^{-n} s^{-1}	8.57e−28	7.13e−18	6.52e−16	5.33e−19
Stress exponent (n)		4	3	3.5	3.5
Activation energy (Q_{disl})	J mol^{-1}	223e3	345e3	530e3	480e3
Activation volume (V_{disl})	m^3 mol^{-1}	0	0	18e−6	11e−6
Diffusion creep					
Material constant (A_{diff})	Pa^{-1} s^{-1}			2.37e−15	1.50e−18
Activation energy (Q_{diff})	J mol^{-1}			375e3	335e3
Activation volume (V_{diff})	m^3 mol^{-1}			10e−6	4e−6
Grain size (d)	m			5e−3	5e−3
Grain size exponent (m)				3	3
Strain weakening					
Angle of internal friction (ϕ)	°	30–15	30–15	30–15	30–15
Cohesion (C)	Pa	20e6–10e6	20e6–10e6	20e6–10e6	20e6–10e6
Strain weakening interval		0.5–1.5	0.5–1.5	0.5–1.5	0.5–1.5
Strain weakening factor		0.5	0.5	0.5	0.5

Note. The material constants for both dislocation and diffusion creeps are modified by the strength parameter f to scale the effective viscosity of the upper plate margin. The rheological parameters are obtained from a combination of previous laboratory (Gleason & Tullis, 1995; Hirth & Kohlstedt, 2003; Rybacki et al., 2006) and numerical studies with a similar setup (Gouiza & Naliboff, 2021; Heron et al., 2023; Naliboff et al., 2017).

$$T(z) = T_t + \frac{q}{k}z - \frac{Hz^2}{2k} \tag{20}$$

where T is the temperature, z the depth, T_t the temperature at the top layer surface, q the top surface heat flux, k the thermal conductivity, and H the rate of internal heat production. For a multi-layered lithosphere, the temperature T_{i+1} and heat flux q_{i+1} at the bottom of each layer can be determined from T_i and q_i at the top surface of that layer (Hasterok & Chapman, 2011):

$$T_{i+1} = T_i + \frac{q_i}{k_i}(z_{i+1} - z_i) - \frac{H_i(z_{i+1} - z_i)^2}{2k_i} \tag{21}$$

$$q_{i+1} = q_i - H_i(z_{i+1} - z_i) \tag{22}$$

Table 2 lists of the parameters used to produce the initial geotherm, and Figures 3d and 3e show the initial geotherm and affected yield strength, respectively. The temperature has no horizontal variations initially but is allowed to evolve once the model run begins. Temperatures at the top and bottom model boundaries are fixed, while the side walls have zero net heat flux.

Table 2
Thermal Properties Used for Constructing the Initial Temperature Profile

Properties	Units	Upper crust	Lower crust	Mantle lithosphere	Asthenosphere
Thickness (Δz)	m	20e3	20e3	80e3	480e3
Top surface temperature (T_t)	K	273	633	881	1,579.67
Top surface heat flow (q)	W m^{-2}	55e−3	35e−3	27e−3	25.4e−3
Thermal conductivity (k)	W m^{-1} K^{-1}	2.5	2.5	3.0	57.15
Internal heat production rate (H)	W m^{-3}	1e−6	4e−7	2e−8	0
Cold lithosphere					
Top surface temperature (T_t)	K	273	583	781	1,479.67
Top surface heat flow (q)	W m^{-2}	48.75e−3	28.75e−3	27e−3	37.31e−3
Hot lithosphere					
Top surface temperature (T_t)	K	273	683	981	1,679.67
Top surface heat flow (q)	W m^{-2}	61.25e−3	41.25e−3	27e−3	13.49e−3

Note. The temperatures at the top and bottom boundary for all models are 273 and 1793 K, respectively. The high value of the asthenospheric thermal conductivity is only used for calculating the initial geotherm in order to account for the reduced rate of temperature increase below the lithosphere-asthenosphere boundary. For all other calculations, the thermal conductivity of the asthenosphere is 3 W m^{-1} K^{-1}.

To minimize model instability given the large viscosity contrast (up to 10^8 Pa s), we apply ASPECT's harmonic averaging scheme for all material fields (Glerum et al., 2018):

$$\mu = \frac{\sum_{i=1}^{a} c_i}{\sum_{i=1}^{a} \frac{c_i}{\mu_i}} \tag{23}$$

where a is the number of compositional fields in the domain, c_i is the contribution of the compositional field, and μ denotes the material field property (e.g., density). To maintain sharp viscosity boundaries between material fields, we apply ASPECT's maximum composition scheme for the effective viscosity, which determines plastic yielding based on the dominant material composition within each cell.

2.5. Parameter Testing

From the reference model, we systematically test eight physical parameters to quantify their impact on the fragment formation (Table 3). The geometry of the weakened upper plate margin is defined by the dip angle of the old plate boundary θ and the lateral extent of the upper plate margin l. Its rheological weakness, in contrast to the

Table 3
Tested Physical Parameters and the Settings for Each

Parameter	Tested settings	Results
Dip angle of the old plate boundary (θ)	15°, **30°**, 45°, 60°, 75°, 90°	Figure 5
Initial extent of the deformation zone (r)	200 km, 300 km, **400 km**	Figure 6
Initial extent of the upper plate margin (l)	200 km, **300 km**, 400 km	Figure 7
Initial geotherm (T_{Moho})	Cold (781 K), **typical (881 K)**, hot (981 K)	Figure 8
Rheologically deformed layer	Nothing, crust-only, mantle lithosphere-only, **whole lithosphere**	Figure 9
Initial plastic strain of the deformation zone (ε_{pl}^0)	Zero, 0.25–0.75, **0.5–1.5**	Figure 10
Extension velocity per side (v)	2.5 mm yr^{-1}, **5 mm yr^{-1}**, 10 mm yr^{-1}	Figure 11
Strength parameter for the upper plate margin (f)	0.05, 0.1, 0.3, **0.5**, 0.7, 0.9, 1, 2, 5	Figure 12

Note. The settings for the reference model (Figure 4) are indicated in bold. The initial geotherm profiles are shown in Table 2 and Figure 3d.

surrounding lithosphere, is quantified by the strength parameter f. The influence of f from 0.1 to 0.9 in increments of 0.2 is evaluated for all the other variables. The lateral extent of the deformation zone r is used to adjust its geometry, and its pre-existing weakness is tested by adjusting the range of the initial plastic strain ε_{pl}^{0} that imposes strain weakening. Furthermore, the crustal and mantle lithospheric layers in which deformation is inherited, the initial geotherm, and the extension velocity are also examined.

2.6. Automated Data Analysis

Given the large number of tested models (94; see Table 3) and model outputs (50–120 model time stamps at an interval of 0.5 Myr), we implement an automated processing system using Python 3.9 (Rossum & Drake, 2010) and ParaView 5.11 (Hansen & Johnson, 2005) to detect the time of continental breakup and the width of the separated fragment. The system approaches in two parts: first identifying a successful continental breakup, where the asthenospheric rocks are uplifted to the model surface. The following criteria are checked in each model time stamp:

1. Identify where the asthenosphere is located for a composition threshold of $c_{as} \geq 0.001$.
2. Identify where the asthenosphere location overlaps with the minimum temperature value (indicating the top surface boundary condition).

Upon satisfying the above criteria, the system records the time stamp at the instant of continental breakup, and the following criteria are used for detecting a continental fragment:

1. Identify where the upper crust is located for a compositional threshold of $c_{uc} \geq 0.5$.
2. Identify where this upper crust location overlaps with the minimum temperature value (indicating the top surface boundary condition).
3. Identify where the surface of this upper crust is moving with a positive horizontal velocity (indicating the motion of a composition away from the rift).
4. After selecting the surface, the system calculates the absolute difference between the minimum and maximum points at the x-axis to determine the fragment width (e.g., Figure 3d).

The automated sequence described above provides the time of continental breakup and the width of the continental fragment by analyzing over 5,000 output files in three separate variables. This procedure allows for a systematic and consistent analysis of fragment formation (as opposed to manual measurements) while reducing the time of analysis by over 90% (e.g., 420 vs. 15 s for a manual and automated measurement using our setup, respectively). This coupled ParaView and Python sequence is provided in the supplementary material (Yu, 2025).

3. Results

3.1. Formation of a Continental Fragment

We present rift models that successfully create a continental fragment and analyze the influence of each parameter on the width of the separated fragment and the time of the continental breakup. The continental fragment selections are outlined in white, with their measured width marked above (Figures 4–12). As shown in the reference model (Figure 4), the continental lithosphere evolves in four stages of deformation:

Stage 1 shows widespread normal faulting due to stretching (Figures 4a and 4d).

In Stage 2, strain is preferentially localized within the weaker upper plate margin, within which marks the locus of rifting. Strain localization is evident through the propagation of faults in the brittle parts of the lithosphere and the coalescence of viscous strain in the ductile parts (Figures 4b and 4f). Rift valleys and small depressions begin to form (Figures 4b and 4f). The fault networks eventually converge to one or a few dominant pairs of low-angle detachment faults directed to a well-defined rift locus (Figures 4b and 4f). The rift locus is controlled by strain localization within both the brittle and viscous regimes.

In Stage 3, the lithosphere significantly thins along the rift locus (Figures 4c and 4g). A large central depression and a small asthenospheric upwelling emerge above and below the rift locus, respectively (Figures 4c and 4g).

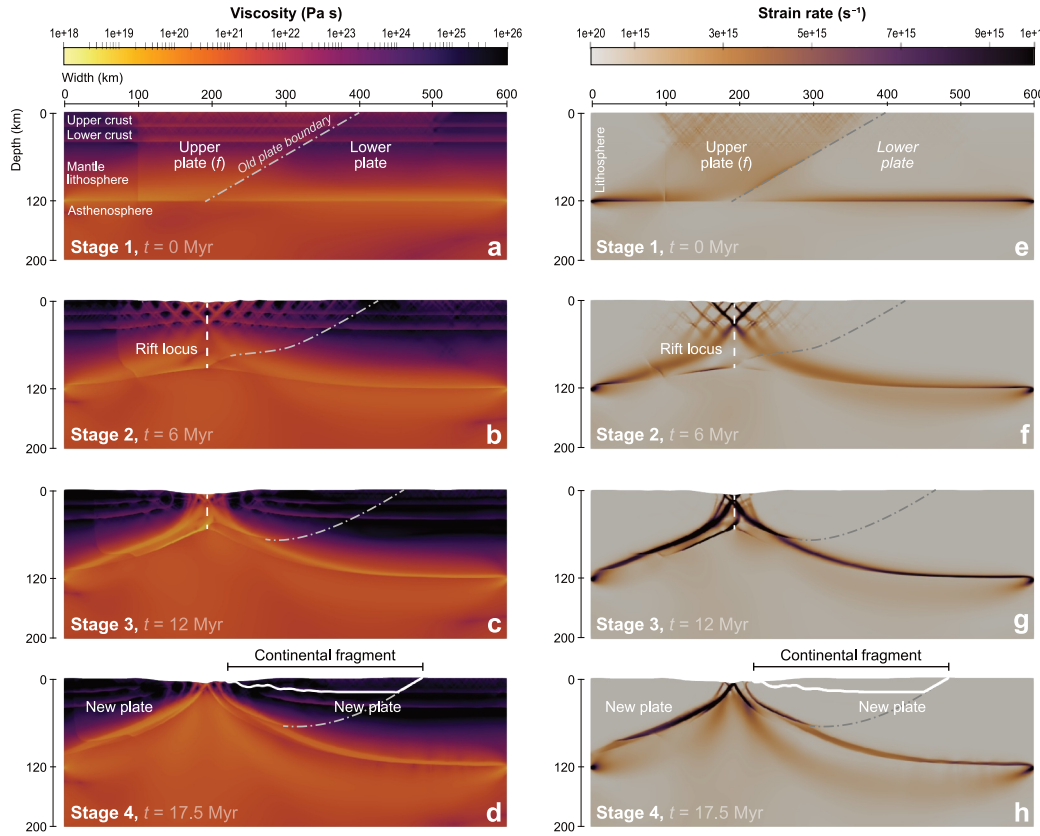

Figure 4. The reference model illustrates the four distinct stages of rifting and the eventual formation of a continental fragment (white outline). (a), (e) Initial viscosity and strain rate profile of the lithosphere in the reference model. The upper plate margin is further weakened by $f = 0.5$. (b), (f) Strain localization of brittle and ductile strain toward the weaker upper plate margin, within which marks the rift locus. (c), (g) Localized lithospheric thinning along the rift locus, accompanied by a distinct asthenospheric upwelling. (d), (h) Instant of continental breakup where the asthenosphere reaches the surface, clearly separating a continental fragment.

Finally, in Stage 4, continental breakup occurs when the lithosphere completely thins. The asthenospheric upwelling ascends along the rift locus and ruptures through the lithosphere (Figures 4d and 4h), severing a continental fragment from the initially weakened upper plate margin, which is now stranded to the lower plate margin (Figures 4d and 4h). The reference model generates a 263.5 km-wide continental fragment—a lithospheric domain between the old plate boundary and the ocean-continent transition of the newly formed rift margin (Figures 4d and 4h).

3.2. Influence of Initial Weakness Geometry

From the reference model, the geometries of the upper plate margin and the deformation zone are tested for their tectonic influence (Figures 5–7). In Figure 5, we examine the dip angle of the old plate boundary θ (Figure 5a). Between $\theta = 15°$ and 45°, a steeper dip angle positions the rift locus closer to the old plate boundary, resulting in a narrower fragment upon breakup (Figures 5b–5d). The difference in fragment widths is much greater between $\theta = 15°$ and 30° (29.9 km on average) than between $\theta = 30°$ and 45° (7.9 km). The general trend is not consistent between $\theta = 45°$ and 90°, where more random variations in fragment widths are observed (Figure 5e).

The strength parameter f does not significantly affect the fragment width, except with a very ductile upper plate margin when $f = 0.1$. In that case, the lithosphere of the upper plate margin undergoes a prolonged period of delocalized thinning, with multiple rift loci competing for strain localization. When $f = 0.1$, θ is instead positively correlated with the fragment width (Figure 5e), and the breakup time for all models increases significantly

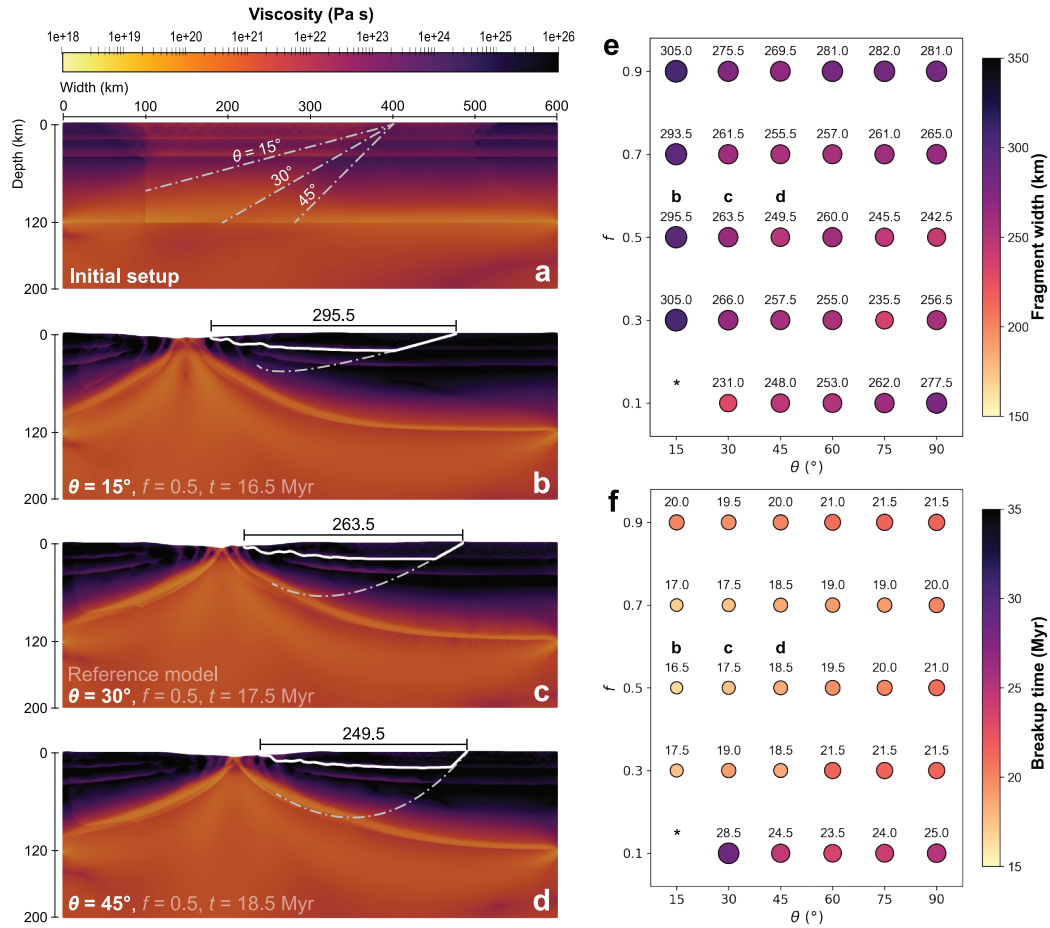

Figure 5. (a) Initial setup showing the continental suture at various dip angles of the old plate boundary θ. (b)–(d) Instant of breakup when $\theta = 15°$, 30°, and 45°, with fragment selection and width measurement. (e) Influence of θ and f on the separated fragment width. (f) Influence of θ and f on the continental breakup time. * denotes that the model fails to fully separate a fragment (i.e., the breakup requirement has not met).

(Figure 5f). Overall, varying θ results in up to ~50 km of difference in fragment widths (Figure 5e). Additionally, higher θ values linearly increase breakup time in most models, with a range difference of ~4 Myr (Figure 5f).

In Figure 6, we explore the impact of the extent of the deformation zone r, which defines the area of rock weakened by the initial plastic strain across both plate margins (dashed in Figure 6a). While keeping the upper plate margin the same as in the reference model, a larger r allows the rift locus to develop further from the old plate boundary, thereby producing a wider fragment upon breakup (Figures 6b–6e). The difference in fragment widths is more profound between $r = 200$ and 300 km (43.625 km on average) than between $r = 300$ and 400 km (14.875 km). However, r does not significantly affect the breakup time (Figure 6f). The general trend is unclear when $f = 0.1$, due to the lack of successful models (Figure 6f).

The extent of the upper plate margin l defines the area of rheologically weakened rock in the upper plate margin via the strength parameter f (dashed in Figure 7a). While keeping the deformation zone the same as in the reference model, a larger l produces a wider fragment (Figures 7b–7e). Similarly, the difference in fragment widths is more pronounced between $l = 200$ and 300 km (66 km on average) than between $l = 300$ and 400 km (19.5 km), except at low f values (0.1 and 0.3). However, l does not significantly influence the breakup time (Figure 7f).

3.3. Influence of Initial Geotherm

In Figure 8, we explore the effects of the initial temperature profile, with particular focus on the Moho temperature. The depth of the brittle-ductile transition is modified by the initial geotherm throughout the lithosphere,

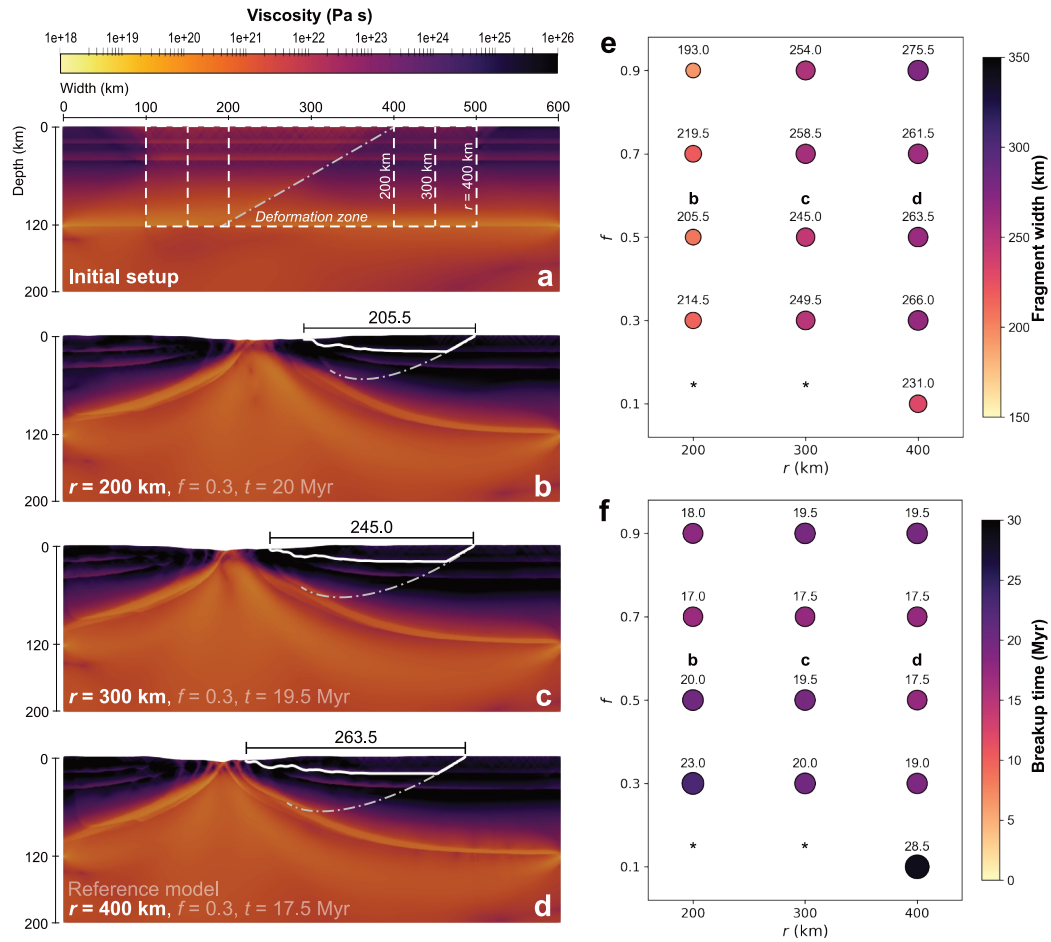

Figure 6. (a) Initial setup showing the continental suture at various extents of the deformation zone *r*. (b)–(d) Instant of breakup when $r = 200$, 300, and 400 km (reference). (e) Influence of *f* and *r* on fragment width. (f) Influence of *f* and *r* on breakup time. * denotes that the model fails to fully separate a fragment.

and further by the strength parameter *f* in the upper plate margin. This changes the mechanical coupling between the brittle and ductile regimes in the lithosphere (Figure 3e).

The models show that a colder, more brittle lithosphere swiftly localizes the strain toward a singular rifting locus, thereby resulting in a narrower rift (Figures 8a and 8b). In contrast, a hotter, more ductile lithosphere promotes distributed faulting with multiple rift loci, leading to a wider rift (Figures 8c and 8d). In addition, higher initial geotherms lead to an increased breakup time (Figures 8e and 8f).

3.4. Influence of Crustal or Mantle Lithospheric Inheritance

In Figure 9, we investigate the role of inheritance in the crust and mantle lithosphere by applying the strength parameter *f* to one or more layers, while keeping the deformation zone the same (Figure 9a). The reference model, with the whole lithosphere deformed, produces a fragment width that falls between those of the crust-only and mantle lithosphere-only models (Figures 9b–9d).

When no rheological inheritance is applied (i.e., only the initial plastic strain acts as an inherited structure, $f = 1$), a pair of competing rifts emerge at the lateral boundaries of the deformation zone, eventually creating a fragment from the upper plate margin after a significantly longer time frame (Figure 9e).

Here, the fragment widths in crust-only models across different *f* values show larger variation (64.5 km) than mantle lithosphere-only (21.5 km) and the whole lithosphere models (44.5 km; Figure 9f). Except when $f = 0.1$,

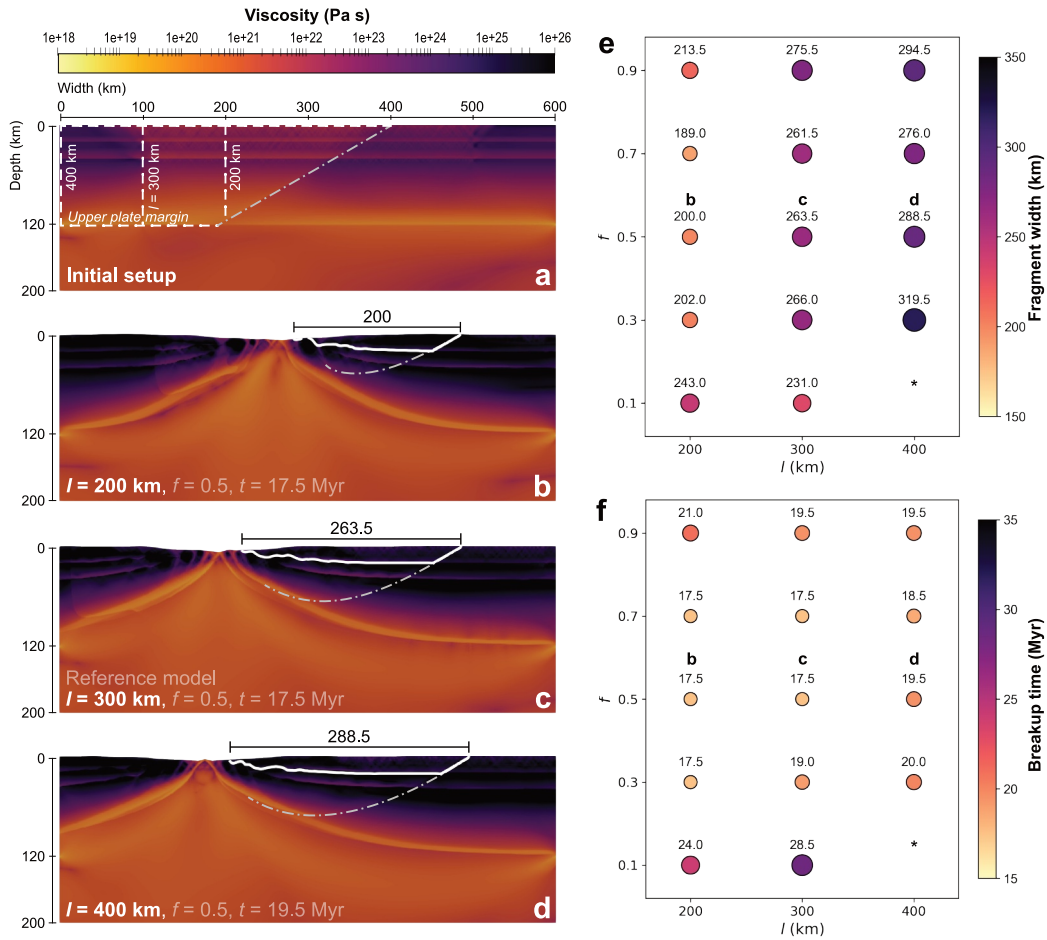

Figure 7. (a) Initial setup showing the continental suture at various widths of the upper plate margin l. (b)–(d) Instant of breakup at $l = 200$, 300 (reference), and 400 km. (e) Influence of f and l on fragment width. (f) Influence of f and l on breakup time. * denotes that the model fails to fully separate a fragment.

the whole lithosphere models align more closely with the mantle lithosphere-only models for both the fragment width and breakup time (Figures 9f and 9g). In addition, the crust-only models have slightly longer breakup times than the others (Figure 9g).

3.5. Influence of Initial Plastic Strain

In Figure 10, we assess the influence of the initial plastic strain ε_{pl}^{0} in the deformation zone by adjusting its base value and the range of random variation. Without any initial strain, the lithosphere in the upper plate margin is consistently thinned away from the old plate boundary (Figure 10a). The fragment widths across different f values are more consistent within the initial strain interval 0.5–1.5 (showing a variation of 44.5 km, with the most notable difference at $f = 0.1$) compared to the other intervals (Figure 10d). Furthermore, the initial plastic strain shortens both the fragment width and breakup time (Figures 10d and 10e).

3.6. Influence of Extension Velocity

In Figure 11, we adjust the extension velocity v at the lateral boundaries. In general, v has minimal effect on the fragment width (Figures 11a–11d). The variation in fragment widths due to f is the lowest at $v = 10$ mm yr^{-1} (10 km), compared to $v = 2.5$ (34 km) and 5 mm yr^{-1} (44.5 km). Furthermore, v is negatively correlated with the breakup time (Figure 11e), with the time difference being much greater between $v = 2.5$ and 5 mm yr^{-1} (~27.8 Myr) than between $v = 5$ and 10 mm yr^{-1} (5.4 Myr).

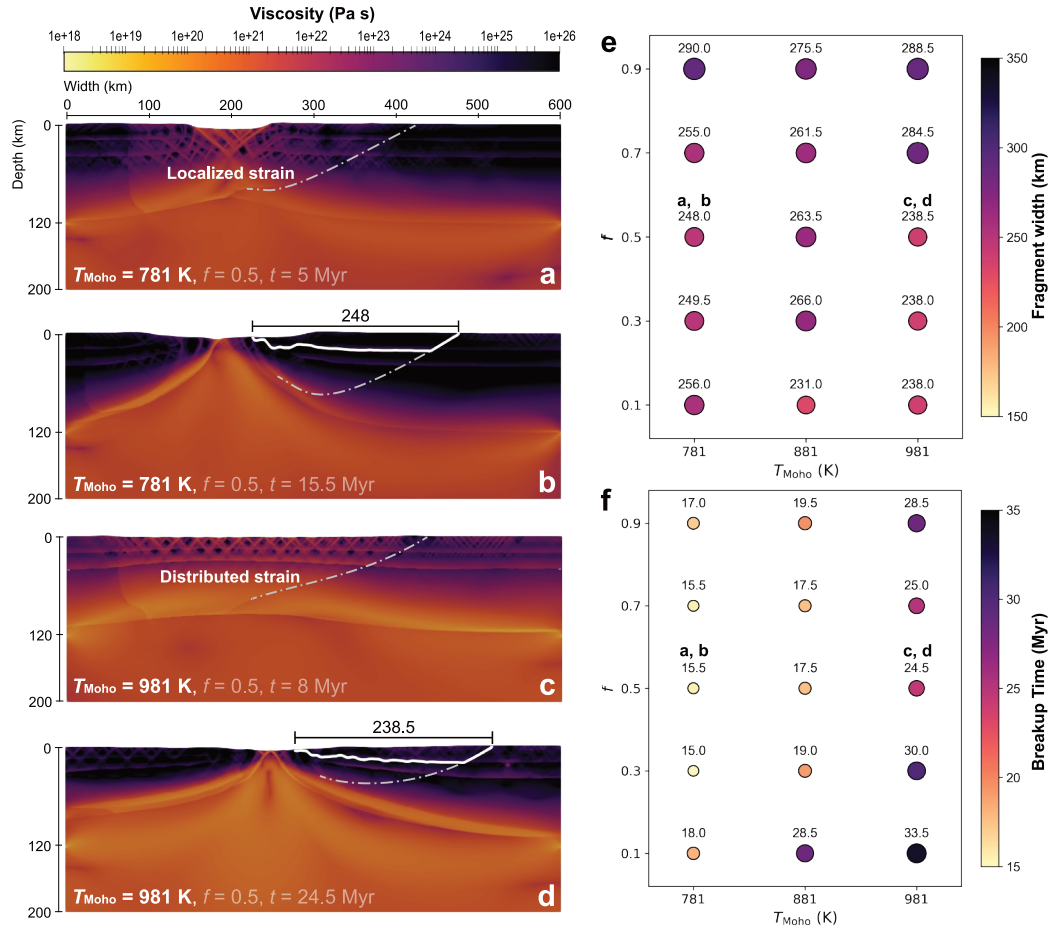

Figure 8. (a–d) Strain localization between a cold (T_{Moho} = 781 K) and hot lithosphere (981 K) and their instant of breakup. Note that the hot lithosphere is further thinned due to delocalized thinning. (e) Influence of f and the initial geotherm on fragment width. (f) Influence of f and the initial geotherm on breakup time.

3.7. Influence of Strength Parameter

As shown in Figures 5–11, the strength parameter f alone, between values of 0.3 and 0.9, does not exert significant control over the fragment width or breakup time. When $f = 0.1$, the mantle lithosphere is entirely ductile, leading to a long period of distributed strain and delocalized thinning during strain localization. In this case, no clear trend is observed between the initial weakness geometry and the resulting fragment width. When $f = 0.05$, the model fails to fully separate a fragment due to the rift migrating to the left model boundary. Finally, when $f > 1$ (i.e., the upper plate margin is stronger than the lower plate margin), strain localizes within the relatively weaker lower plate, and the fragment forms in the lower plate margin instead (Figures 12b and 12c).

4. Discussion

4.1. Key Controlling Parameters

The models produce continental fragments ranging in widths of ~175–350 km, formed from predominantly the upper plate, over a period of ~15–35 Myr (Figure 13). They show that fragment formation occurs due to localized strain weakening at an offset away from the old plate boundary. The locus of rifting is determined by the interplay between the brittle and ductile weakening processes, guided by pre-existing plastic and viscous inheritances related to earlier closure.

Most importantly, the geometry of the inherited structures, in the form of the dip angle of the old plate boundary θ, the extent of the rheologically weakened upper plate margin l, as well as the extent of the plastic strain-weakened

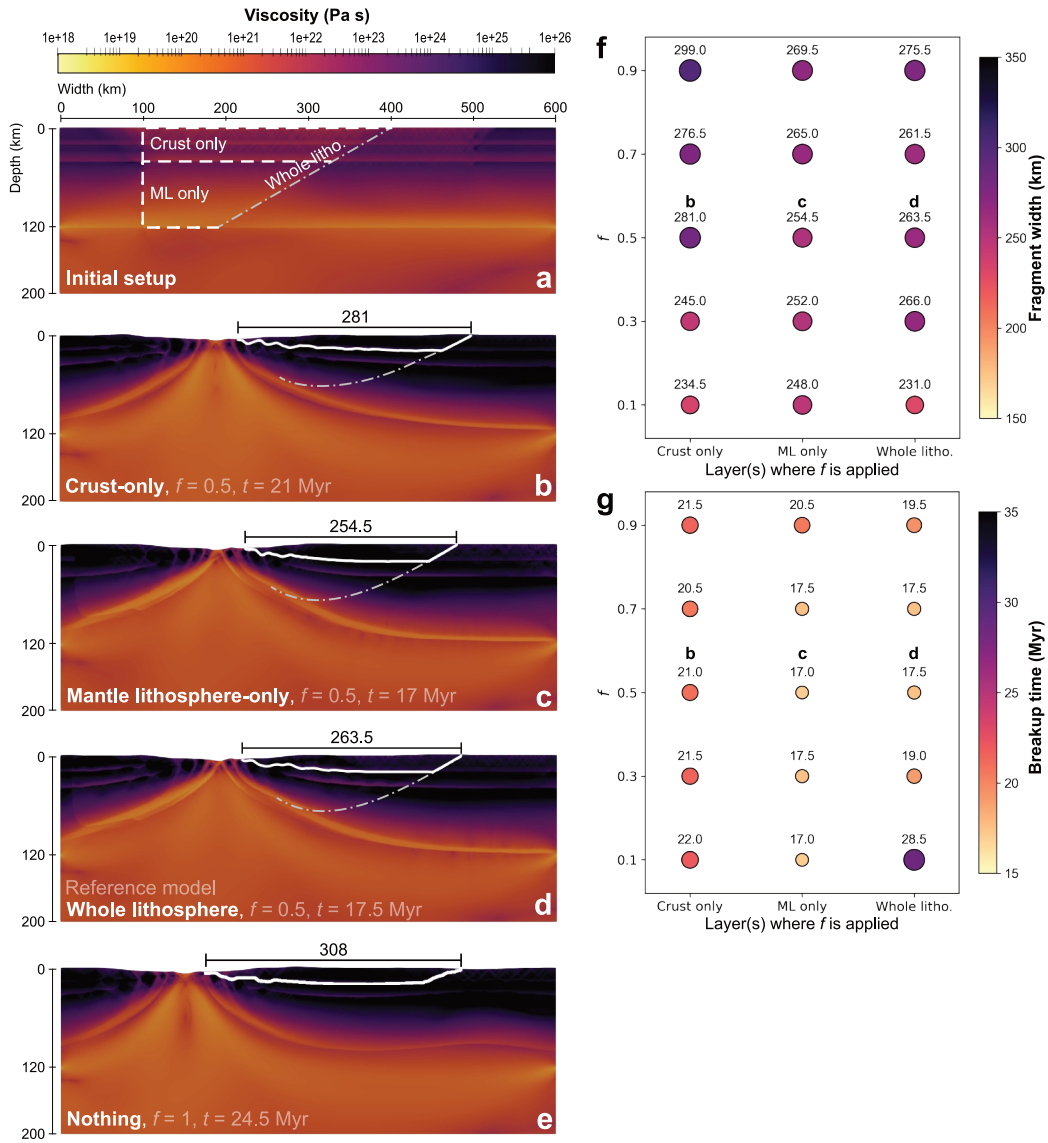

Figure 9. (a) Initial setup showing the continental suture where f is applied to crust only, mantle-lithosphere only, whole lithosphere, or nothing. (b)–(e) Instant of breakup with various setups of crustal and/or mantle lithospheric inheritance. (f) Influence of f and applied layers on fragment width. (g) Influence of f and applied layers on breakup time.

deformation zone r, determines where rifting occurs and, consequently, the width of the resulting fragment (Figures 5–7).

The magnitude of plastic and viscous inheritance, represented by ε_{pl}^{0} and f, activate strain localization. Both parameters can significantly speed up the fragment formation process but neither directly controls the width of the resulting fragment except at extreme values (Figures 10 and 12). Notably, a stronger upper plate margin when $f > 1$ produces a fragment in the lower plate margin instead (Figure 12c).

However, a ductile lithosphere, due to either highly imposed rheological weakening or an elevated geotherm, results in a shallower depth of brittle-ductile transition for all crustal and mantle lithospheric layers. Such condition prolongs strain localization, creating distributed strain and a wider rift (Figure 8). Consequently, no clear trend is observed between the initial weakness geometry and fragment width due to the non-linearity of ductile deformation. In some cases, models with a very ductile upper plate margin can even fail, as the rift locus migrates toward the left model boundary, preventing further separation of the upper plate fragment.

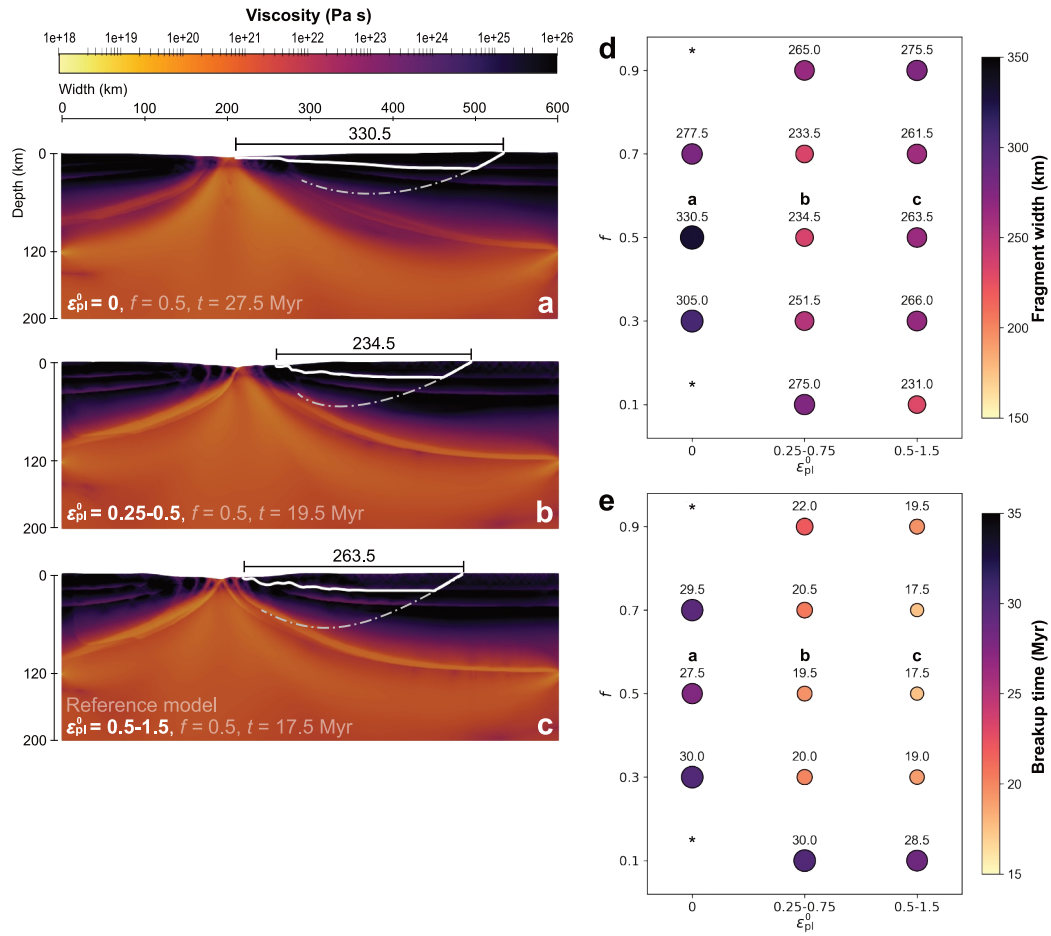

Figure 10. (a–c) Instant of breakup with the initial plastic strain ε^0_{pl} in various intervals of zero, 0.25–0.5, and 0.5–1.5 (reference) in the deformation zone (see Figure 3a). (d) Influence of f and ε^0_{pl} on fragment width. (e) Influence of f and ε^0_{pl} on breakup time. * denotes that the model fails to fully separate a fragment.

Both crustal and mantle lithospheric inheritance exert influence on the rift locus, but the mantle lithosphere exerts a stronger control due to its greater yield strength (Figure 9). The greater variability in fragment widths observed when only the crust is weakened can be attributed to the geometry of the upper plate margin and to the stronger influence of randomized initial plastic strain on strain localization (Figure 9).

Extension velocity controls the rate of strain buildup and consequently the timing of breakup, but it does not strongly influence the rift locus and fragment width (Figure 11). The overall influence of the fragment width is more related to the geometry and extent of the inherited deformation within the lithosphere, rather than the external impact of extension velocity.

4.2. Comparison to Geological Examples

Figure 1 provides the geological context for exotic continental fragments, and Figure 13a compares their widths with our modeled results. Specifically, the breakup of Pangea and the opening of the South Atlantic, North Atlantic, and Indian Oceans left behind several fragments: the São Francisco Craton in eastern South America (Aguilar et al., 2017), the São Luís Craton in northern Brazil (Klein & Moura, 2008), the Nain Province in eastern Canada (Bridgwater et al., 1973), the Lewisian Complex in northwestern Scotland (Park, 2022), Madagascar (Agrawal et al., 1992), and the Napier Complex in eastern Antarctica (Mohanty, 2011; Figure 1). These fragments are composed primarily of Archean-to-Paleoproterozoic nuclei, juxtaposed by younger orogenic belts and sedimentary basins (Agrawal et al., 1992; Bridgwater et al., 1973; Klein & Moura, 2008; Mohanty, 2011; Teixeira

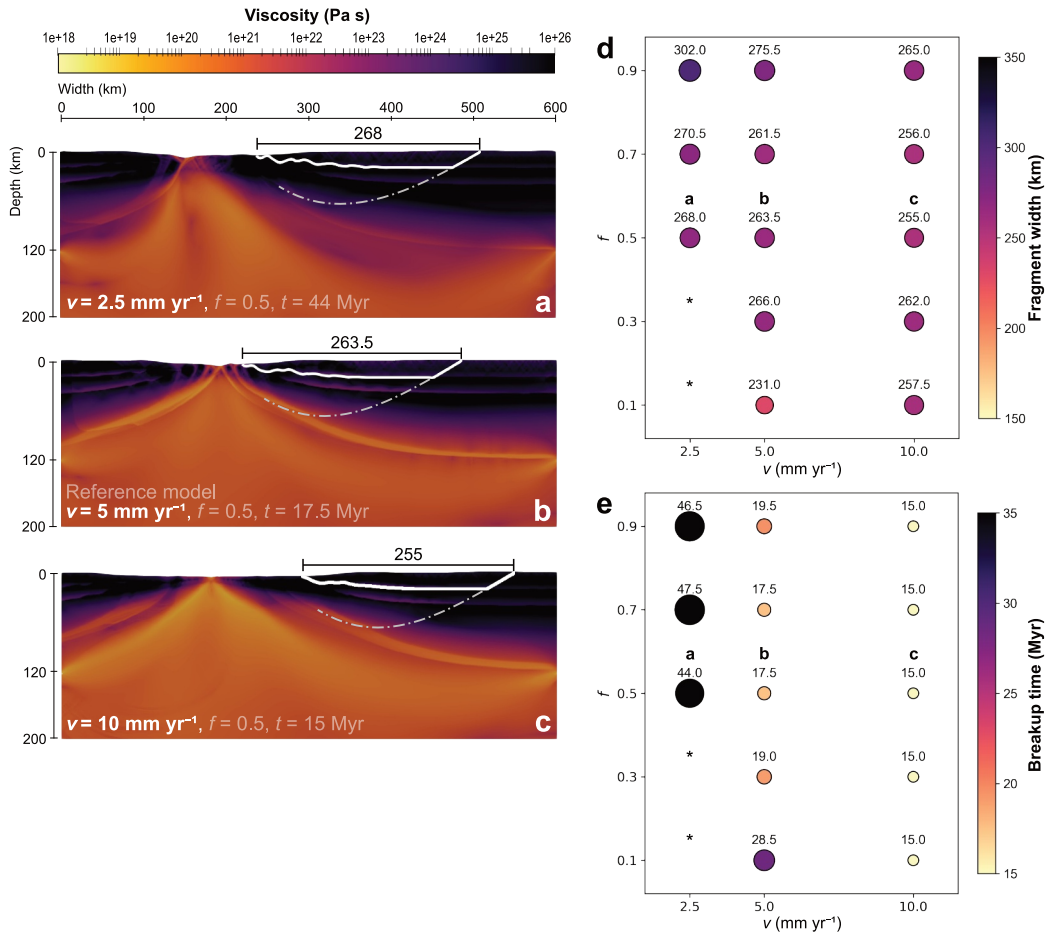

Figure 11. (a–c) Instant of breakup with the extension velocity v set to 2.5, 5 (reference), and 10 mm yr^{-1}. (d) Influence of v and f on fragment width. e) Influence of v and f on breakup time. * denotes that the model fails to fully separate a fragment.

et al., 2017; Wheeler et al., 2010). As discussed below, they also exhibit a common history of subduction, collision, and intraplate deformation in previous Wilson Cycles.

The South Atlantic Rift (~160 Ma) followed old sutures that define South America and Africa but separated the São Francisco and later the São Luís fragment from western Africa (Figure 1; Brune et al., 2018; Buiter & Torsvik, 2014; Klein et al., 2005; Klein & Moura, 2008). Before their separation, the surrounding lithosphere of these fragments had endured deformation from at least two Wilson Cycles: the Paleoproterozoic Trans-Amazonian Orogeny (~2.1–1.9 Ga; Hurley et al., 1967; Klein & Moura, 2008; Teixeira et al., 2017) and the Neoproterozoic Pan-African/Brasiliano Orogeny (~600–400 Ma; Pedrosa-Soares, 2001).

The Trans-Amazonian Orogeny established a Paleoproterozoic connection—often described as a cratonic bridge—between eastern São Francisco and western Congo (Figure 1; Aguilar et al., 2017; Alkmim, 1998). The region then underwent prolonged extension without fully separating, followed by convergence and the Pan-African/Brasiliano Orogeny that formed the West Gondwana supercontinent (Figure 1; Konopásek et al., 2020; Teixeira et al., 2017). However, the South Atlantic Ocean opened subparallel to the north-south ancient sutures from both orogenies but did not continue further into northwestern Africa (Figure 1), instead proceeding almost orthogonally, in an east-west direction toward São Luís (De Wit et al., 2008; Heine & Brune, 2014). The rather large width of the São Francisco fragment (~300–800 km) is outside of the modeled range (Figure 13a), suggesting that its formation may involve processes not captured by our models. However, the reactivation of subparallel Brasiliano sutures to its south likely played a major role in its fragmentation (Figure 1; Pedrosa-Soares, 2001).

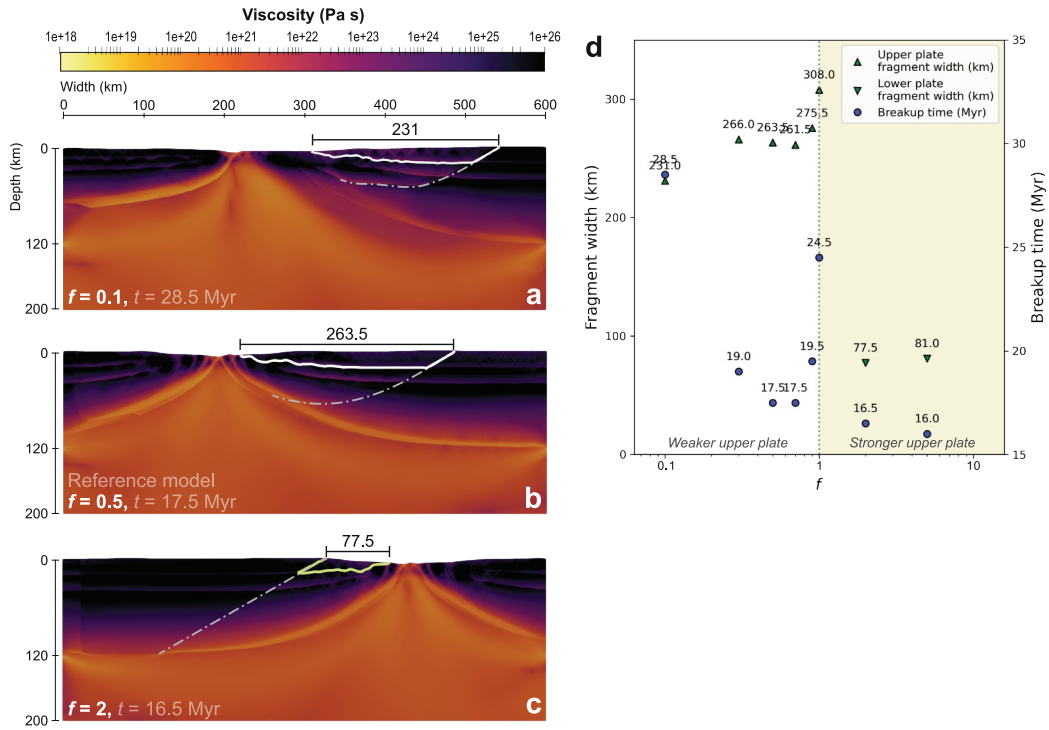

Figure 12. (a–c) Instant of breakup with the strength parameter f set to 0.1, 0.5 (reference), and 2. (d) Influence of f on both fragment width and breakup time. With a stronger upper plate margin (shaded beige), the fragment forms in the lower plate margin instead.

The São Luís Craton was involved in an accretionary setting during the Trans-Amazonian Orogeny (Klein et al., 2005). Along its southern margin, the Gurupi Orogen (Figure 1; ~750–550 Ma) records the suture site of both Trans-Amazonian and Brasiliano Orogenies (Klein & Moura, 2008). However, despite the presence of complex crustal deformation in the Gurupi Orogen, the South Atlantic Rift developed north of São Luís. The São Luís fragment has a width of ~150–200 km, consistent with the model-predicted range (Figure 13a).

The North Atlantic realm contains two major rift branches: the Labrador Sea–Baffin Bay Rift system (also known as the Northwest Atlantic Rift) and the Northeast Atlantic Rift (Figure 1). The Northwest Atlantic Rift opened the Labrador Sea (~79–60 Ma), which separated North America (and the Nain Province) from western Greenland (Bridgwater et al., 1973; Heron et al., 2023). This rift branch was active for ~20 Myr until the Northeast Atlantic opening in the Early Eocene (~56 Ma), which gained supremacy and separated Eurasia (and the Lewisian Complex) from eastern Greenland (Abdelmalak et al., 2019; Brune et al., 2016; Wheeler et al., 2010).

The Nain Province records a Neoarchean collision (~2.5 Ga) between two continental blocks that formed part of the North Atlantic Craton (Connelly & Ryan, 1996). To its west, a subsequent Paleoproterozoic (~1.9 Ga) subduction occurred, with the Nain Province as the upper plate (Figure 1; St-Onge et al., 2009; Wardle et al., 2002). The consequent collision created the Torngat and New Québec Orogens (~1.9–1.8 Ga), representing a two-sided collision involving the Nain Province to the east, the Churchill Province in between, and the Superior Province to the west (Scott & Machado, 1995; Wardle et al., 1990, 2002). The Labrador Sea did not open along either orogen but instead parallel east of Nain, creating a fragment ~100–150 km wide that falls below the modeled range (Figure 13a). However, a previous modeling study created a tailored tectonic environment by applying a distinct mantle lithosphere scar to produce a fragment within the Nain range (Heron et al., 2023).

The Lewisian Complex, initially part of the North Atlantic Craton, likely experienced an Archean subduction (~3.0–2.7 Ga), as evidenced by widespread dyke intrusions and an accretionary complex (Mason & Brewer, 2004; Sutton & Watson, 1950; Wheeler et al., 2010). The consequent collision, which likely occurred concurrently with the Torngat Orogeny (Peace et al., 2018), formed the Nagssugtoqidian Orogen (Figure 1;

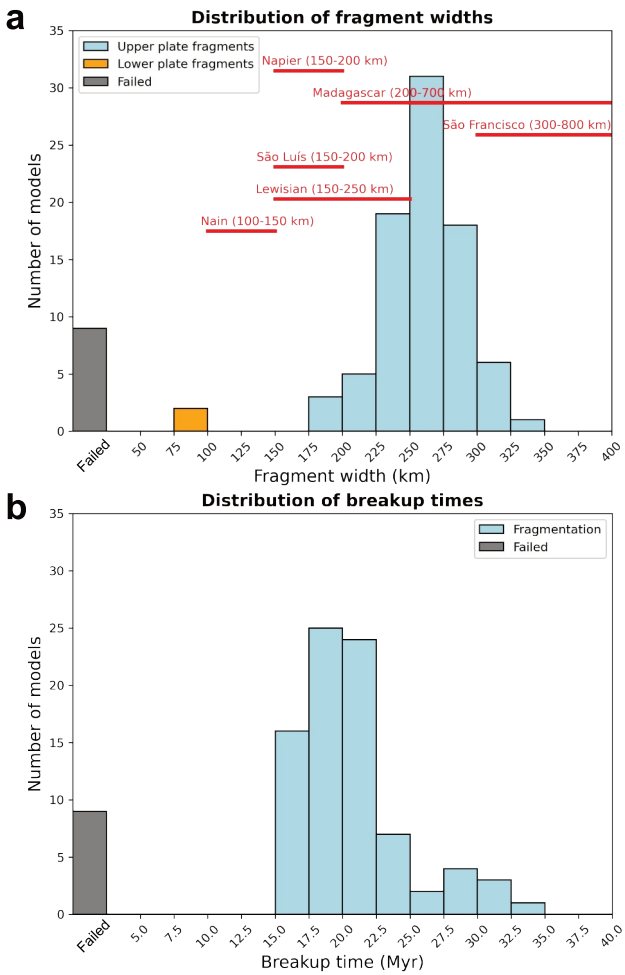

Figure 13. (a) Distribution of fragment widths generated from all models, overlain with the widths of geological examples indicated by red lines. Colors represent upper plate fragments (blue), lower plate fragments (orange), and failed models (gray). (b) Distribution of breakup times generated from all models, with successful fragmentation (blue) and failed models (gray).

~1.9 Ga) that reworked most of the Lewisian (Kolb, 2014; Park, 2022). The Lewisian bedrock was also affected by prolonged metamorphism during the Ketilidian (~1.8–1.7 Ga) and Grenville (~1.2–1.0 Ga) Orogenies (McCaffrey et al., 2004; Park, 2022). During the Caledonian Orogeny (~490–390 Ma), the Iapetus Ocean closed south of the Lewisian Complex in the Scottish Highlands (Figure 1; Buiter & Torsvik, 2014). Northwest of the Lewisian Complex, intraplate rifting commenced in the Late Jurassic (~170 Ma) but ultimately failed (Skogseid et al., 2000). The later Northeast Atlantic Rift developed almost orthogonal to the ancient Nagssugtoqidian suture but subparallel with the Iapetus suture (Figure 1), with local influence from the Ketilidian and Grenville boundaries (McCaffrey et al., 2004; Park, 2022). The Lewisian Complex has a width of ~150–250 km, which is within the modeled range (Figure 13a).

The Dharwar Craton of peninsular India was originally connected to Madagascar to its west and the Napier Complex to its east, all of which formed part of the East Gondwana supercontinent (Agrawal et al., 1992; Collins & Pisarevsky, 2005; Li et al., 2008). Madagascar represents another large fragment with a width of ~200–700 km (Figure 13), as a result of multi-phase extension and the reactivation of multiple surrounding Pan-African sutures (Figure 1; Collins & Windley, 2002; Fritz et al., 2013; Reeves & De Wit, 2000; Schofield et al., 2010). The ~150–200 km-wide Napier Complex aligns with modeled fragments (Figure 13a), having been separated by rifting along the Eastern Ghats (Figure 1; Boger et al., 2001; Collins & Pisarevsky, 2005; Reeves & De Wit, 2000).

4.3. Comparison to Previous Setups

The complexity of suture zone evolution and deformation is well recognized (Bleeker, 2003; Dewey, 1977), making it challenging to model accurately in simulations. Nonetheless, previous numerical models have explored a wide range of idealized weak zones to simulate an old plate boundary.

Heron et al. (2023) suggested that a reactivated sutured scar from an ocean closure during the Torngat orogeny could have controlled the locus of the Labrador Sea rift. In their models, strain localized along the weakened scar at the old plate boundary between two margins, with the position of the scar controlling the resulting fragment width. In contrast, our models did not include any discrete scar-like rheological weakening along the old plate boundary. Although their suture setup produced a fragment comparable to the Nain Province, the modeled fragment widths were limited to ~100–150 km, constrained by the depth to which the suture penetrates through the lithosphere. This may explain the formation of narrower fragments, but the origin of larger ones remains unresolved.

Petersen and Schiffer (2016) incorporated an eclogite slab and a serpentinized mantle wedge to represent inherited orogenic weaknesses. Although the geometry of the eclogite slab was similar to the scar in the models of Heron et al. (2023), it had a similar rheology to the host mantle lithosphere and therefore did not play a dominant role in localizing strain. Instead, this was controlled by the weaker serpentinized mantle wedge—analogous to the weakened upper plate margin in our model setup. Their models showed that wider fragments (up to 200 km) could form in scenarios with thicker crusts that cause the rift to migrate inland. However, their models only considered deformation in the upper plate, neglecting potential weaknesses that could develop in the lower plate due to collision and orogeny.

Salazar-Mora et al. (2018) imposed prior compression to simulate orogeny before extending the model. Their model, driven by a weak seed, produced widespread crustal shear zones in both plate margins during compression, with the most pronounced development in the lower plate. Upon extension, rifting developed away from the orogenic suture but instead in the lower plate. This is different from our observation in which the fragment

developed in the weakened upper plate margin. The amount of compression affects the width of the reactivated crustal segment, its distance from the suture, and thereby the width of the separated fragment. However, their setup did not incorporate any subduction-related deformation.

Gouiza and Naliboff (2021) examined the role of large-scale rheological inheritance in the Labrador Sea rift. Though they used a zone of initial strain to initiate rifting, the lithospheric strength was modified through the initial geotherm and rheology of the crust and mantle lithosphere. Their models showed that a colder, more brittle lithosphere with a strong lower crust produces a narrower and symmetric rift, whereas a hotter, more ductile lithosphere results in prolonged crustal thinning, asymmetric rifting, and a wider fragmented crust. This aligns with our findings when adjusting the initial geotherm.

To expand the modeling work on fragment formation, we integrate elements from both Petersen and Schiffer (2016) and Gouiza and Naliboff (2021). The geometry and yield strength of the upper plate margin and deformation zone are quantified to account for uncertainties related to subduction and collision in previous Wilson cycles. As a result, this study provides a more comprehensive analysis of the suture zone complexity for fragment formation.

4.4. Model Limitations and Future Work

The modeling work offers a first analysis into a wide range of physical parameters that may influence fragment formation during rifting. However, a more tailored approach to specific geological examples may gain further regional insights (e.g., Glerum et al., 2020; Gouiza & Naliboff, 2021; Neuharth et al., 2021). Future studies could focus on adding local geological constraints and data, such as the deformation extent, duration and velocity of rifting, and testing specific regional settings in three-dimensional (3-D) models.

The extension velocity is applied horizontally, whereas rifting is often oblique in nature (Brune et al., 2018). Therefore, 3-D models can better capture the complexity of inherited structures and deformation patterns caused by plate motions throughout the rift (e.g., Van Wijk, 2005; Xue et al., 2024). In addition, more complex plate motions can be modeled, such as convergence followed by extension (e.g., Salazar-Mora et al., 2018) or multi-phase extensions with a long hiatus in between (e.g., Naliboff & Buiter, 2015). A notable case to model is the separation of the São Francisco Craton, characterized by the multi-phase, multi-directional rifts between South America and Africa (e.g., Brune et al., 2016).

The fragment width is used as a first-order geological constraint here. However, some of the models show that crustal fragments can undergo significant stretching and thinning under extension, especially with a hotter, more ductile lithosphere. Thus, improvements can be made in fragment width measurement by calculating the stretch factor (e.g., Gün et al., 2024; McKenzie, 1978). Furthermore, associating the modeled crustal expression with geological domains along the rifted margins can offer improved surficial constraints (e.g., Gouiza & Naliboff, 2021).

Though we simulate inherited weaknesses that account for deformation processes through both strain and rheological modifications, it is crucial to acknowledge the limitations regarding modeling syn-rift processes such as melt generation and magma intrusion. Future models could simulate magma intrusion using two-phase flow, though such implementation is computationally expensive and requires further constraints. In addition, an area of future work should focus on timing between deformation and subsequent reactivation of an inherited structure (e.g., Salazar-Mora & Sacek, 2023). For example, implementing a temperature-dependent strain healing mechanism (e.g., Fuchs & Becker, 2019) may offer further insights in the preservation of deformation within the lithosphere in low strain rate settings.

Furthermore, though surface erosion and deposition are applied through a diffusive equation (Equation 19) at the model's top boundary, a more realistic sedimentary loading system can be implemented in future studies using a stream-power law that accounts for fluvial erosion and deposition, hillslope diffusion, and basin infilling (e.g., Neuharth et al., 2022).

Finally, there is ongoing debate regarding whether a mantle plume can initiate a rift, given the almost simultaneous emplacement of large igneous provinces during rifting (Buiter & Torsvik, 2014). Notably, the fragmentation of the Lewisian Complex coincided with the formation of the North Atlantic Igneous Province (Peace

et al., 2020; Vink, 1984). Through active models, future work could investigate the potential role of mantle plumes in fragment formation.

5. Conclusions

To investigate the influence of structural inheritance on continental fragment formation, we conducted a total of 94 numerical 2-D rift models using ASPECT, featuring a rheologically weakened upper plate margin (representing inheritance from previous subduction) within a lithospheric-scale deformation zone of initial plastic strain (representing inheritance from previous collision and orogeny; Figure 3).

We systematically tested eight key parameters, varying the geometry and weakness of the upper plate margin and the deformation zone, the initial geotherm, as well as the extension velocity. To ensure efficient and consistent model analysis, we implemented an automated system that detects the instant of continental breakup and measures the separated fragment width. The models demonstrate that localized strain weakening away from the previous plate boundary can be a primary driver of fragment formation (Figure 4). Most importantly, the geometry of the inherited structures determines the width of the separated continental fragment (Figures 5–7). However, a very ductile lithosphere can prolong the fragment formation process through delocalized thinning, thus introducing significant nonlinearity in resulting fragment widths (Figure 8).

Our models produce continental fragments ranging in widths from ∼175 to 350 km (Figure 13), consistent with geological examples that exhibit one or multiple stages of subduction, collision, and intraplate deformation before rifting (Figure 1). These include the Lewisian Complex, São Luis Craton, part of Madagascar, and Napier Complex. However, the modeled dimensions do not fit well with the Nain Province and the São Francisco Craton. By identifying key first-order factors controlling fragment formation, the work here provides a tectonic recipe for future 3-D regional models with more robust geological constraints.

Acknowledgments
We would like to thank Robert Moucha and an anonymous reviewer, as well as the Associate Editor, for their thoughtful feedback which helped strengthen the paper. AJY thanks the Government of Ontario for funding his research through the Queen Elizabeth II Graduate Scholarship in Science and Technology while the majority of this research was conducted. PJH gratefully acknowledges the support provided by the Digital Research Alliance of Canada (alliancecan.ca) and the Natural Sciences and Engineering Research Council of Canada (NSERC) through an NSERC Discovery Grant (RGPIN-2022-03084). The revision and final editing stage of this paper was completed during AJY's time at the GFZ Helmholtz Centre for Geosciences, supported by the Marie Skłodowska-Curie Actions Doctoral Network TALENTS funded by the European Union (HORIZON-MSCA-2022-DN-01 and No. 101119486), as well as during EG's affiliation with MARUM—Center for Marine Environmental Sciences at the University of Bremen. Computations were performed on the Niagara supercomputer at the SciNet HPC Consortium. SciNet is funded by the Canada Foundation for Innovation, the Government of Ontario, Ontario Research Fund-Research Excellence, and the University of Toronto. We also thank the Computational Infrastructure for Geodynamics, funded by the U.S. National Science Foundation under awards EAR-0949446 and EAR-1550901, for supporting the development of ASPECT.

Conflict of Interest

The authors declare no conflicts of interest relevant to this study.

Data Availability Statement

The ASPECT input file for the reference model, the Python scripts for the initial temperature profile and yield strength envelope, as well as the ParaView Python script for the continental breakup detection and fragment dimension analysis, are openly accessible in a Zenodo repository (Yu, 2025).

References

Abdelmalak, M. M., Planke, S., Polteau, S., Hartz, E. H., Faleide, J. I., Tegner, C., et al. (2019). Breakup volcanism and plate tectonics in the NW Atlantic. *Tectonophysics*, *760*, 267–296. https://doi.org/10.1016/j.tecto.2018.08.002

Agrawal, P. K., Pandey, O. P., & Negi, J. G. (1992). Madagascar: A continental fragment of the paleo-super Dharwar craton of India. *Geology*, *20*(6), 543. https://doi.org/10.1130/0091-7613(1992)020<0543:MACFOT>2.3.CO;2

Aguilar, C., Alkmim, F. F., Lana, C., & Farina, F. (2017). Palaeoproterozoic assembly of the São Francisco craton, SE Brazil: New insights from U–Pb titanite and monazite dating. *Precambrian Research*, *289*, 95–115. https://doi.org/10.1016/j.precamres.2016.12.001

Alkmim, F. F. (1998). Transamazonian orogeny in the southern Sa˜o Francisco craton region, Minas Gerais, Brazil: Evidence for paleoproterozoic collision and collapse in the Quadril´atero Ferri´fero. *Precambrian Research*, *90*(1–2), 29–58. https://doi.org/10.1016/s0301-9268(98)00032-1

Bangerth, W., Dannberg, J., Fraters, M., Gassmoeller, R., Glerum, A., Heister, T., et al. (2022). ASPECT v2.4.0 (Version v2.4.0). *Zenodo*. https://doi.org/10.5281/ZENODO.6903424

Beniest, A., Willingshofer, E., Sokoutis, D., & Sassi, W. (2018). Extending continental lithosphere with lateral strength variations: Effects on deformation localization and margin geometries. *Frontiers in Earth Science*, *6*, 148. https://doi.org/10.3389/feart.2018.00148

Bleeker, W. (2003). The late Archean record: A puzzle in ca. 35 pieces. *Lithos*, *71*(2–4), 99–134. https://doi.org/10.1016/j.lithos.2003.07.003

Boger, S. D., Wilson, C. J. L., & Fanning, C. M. (2001). Early Paleozoic tectonism within the East Antarctic craton: The final suture between east and west Gondwana? *Geology*, *29*(5), 463. https://doi.org/10.1130/0091-7613(2001)029<0463:EPTWTE>2.0.CO;2

Bridgwater, D., Watson, J., & Windley, B. F. (1973). The archaean craton of the North Atlantic region. *Philosophical Transactions of the Royal Society of London - Series A: Mathematical and Physical Sciences*, *273*, 493–512.

Brun, J. –P. (1999). Narrow rifts versus wide rifts: Inferences for the mechanics of rifting from laboratory experiments. *Philosophical Transactions of the Royal Society of London,Series A: Mathematical, Physical and Engineering Sciences*, *357*(1753), 695–712. https://doi.org/10.1098/rsta.1999.0349

Brune, S., Heine, C., Pérez-Gussinyé, M., & Sobolev, S. V. (2014). Rift migration explains continental margin asymmetry and crustal hyperextension. *Nature Communications*, *5*(1), 4014. https://doi.org/10.1038/ncomms5014

Brune, S., Williams, S. E., Butterworth, N. P., & Müller, R. D. (2016). Abrupt plate accelerations shape rifted continental margins. *Nature*, *536*(7615), 201–204. https://doi.org/10.1038/nature18319

Brune, S., Williams, S. E., & Müller, R. D. (2018). Oblique rifting: The rule, not the exception. *Solid Earth*, *9*(5), 1187–1206. https://doi.org/10.5194/se-9-1187-2018

Buiter, S. J. H., & Torsvik, T. H. (2014). A review of Wilson cycle plate margins: A role for mantle plumes in continental break-up along sutures? *Gondwana Research*, *26*(2), 627–653. https://doi.org/10.1016/j.gr.2014.02.007

Cawood, P. A., Hawkesworth, C. J., Pisarevsky, S. A., Dhuime, B., Capitanio, F. A., & Nebel, O. (2018). Geological archive of the onset of plate tectonics. *Philosophical Transactions of the Royal Society A: Mathematical, Physical and Engineering Sciences*, *376*(2132), 20170405. https://doi.org/10.1098/rsta.2017.0405

Cembrano, J., & Lara, L. (2009). The link between volcanism and tectonics in the southern volcanic zone of the Chilean Andes: A review. *Tectonophysics*, *471*(1–2), 96–113. https://doi.org/10.1016/j.tecto.2009.02.038

Chapman, D. S. (1986). Thermal gradients in the continental crust. *Geological Society, London, Special Publications*, *24*(1), 63–70. https://doi.org/10.1144/GSL.SP.1986.024.01.07

Collins, A. S., & Pisarevsky, S. A. (2005). Amalgamating eastern Gondwana: The evolution of the Circum-Indian orogens. *Earth-Science Reviews*, *71*(3–4), 229–270. https://doi.org/10.1016/j.earscirev.2005.02.004

Collins, A. S., & Windley, B. F. (2002). The tectonic evolution of central and northern Madagascar and its place in the final assembly of Gondwana. *The Journal of Geology*, *110*(3), 325–339. https://doi.org/10.1086/339535

Connelly, J. N., & Ryan, B. (1996). Late Archean evolution of the Nain province, Nain, Labrador: Imprint of a collision. *Canadian Journal of Earth Sciences*, *33*(9), 1325–1342. https://doi.org/10.1139/e96-100

Dewey, J. F. (1977). Suture zone complexities: A review. *Tectonophysics*, *40*(1–2), 53–67. https://doi.org/10.1016/0040-1951(77)90029-4

Dewey, J. F., & Bird, J. M. (1970). Mountain belts and the new global tectonics. *Journal of Geophysical Research*, *75*(14), 2625–2647. https://doi.org/10.1029/JB075i014p02625

Dewey, J. F., & Burke, K. (1974). Hot spots and continental break-up: Implications for collisional orogeny. *Geology*, *2*(2), 57. https://doi.org/10.1130/0091-7613(1974)2<57:HSACBI>2.0.CO;2

De Wit, M. J., Stankiewicz, J., & Reeves, C. (2008). Restoring Pan-African-Brasiliano connections: More Gondwana control, less trans-Atlantic corruption. *Geological Society, London, Special Publications*, *294*(1), 399–412. https://doi.org/10.1144/SP294.20

Döhmann, M. J. E. A., Brune, S., Nardini, L., Rybacki, E., & Dresen, G. (2019). Strain localization and weakening processes in viscously deforming rocks: Numerical modeling based on laboratory torsion experiments. *Journal of Geophysical Research: Solid Earth*, *124*(1), 1120–1137. https://doi.org/10.1029/2018JB016917

Dubinin, E. P., Grokholsky, A. L., & Makushkina, A. I. (2018). Physical modeling of the formation conditions of microcontinents and continental marginal plateaus. *Izvestiya–Physics of the Solid Earth*, *54*(1), 66–78. https://doi.org/10.1134/S1069351318010056

Fossen, H., Khani, H. F., Faleide, J. I., Ksienzyk, A. K., & Dunlap, W. J. (2017). Post-caledonian extension in the West Norway–northern north Sea region: The role of structural inheritance. *Geological Society, London, Special Publications*, *439*(1), 465–486. https://doi.org/10.1144/SP439.6

Fraters, M. R. T., Bangerth, W., Thieulot, C., Glerum, A. C., & Spakman, W. (2019). Efficient and practical Newton solvers for non-linear Stokes systems in geodynamic problems. *Geophysical Journal International*, *218*(2), 873–894. https://doi.org/10.1093/gji/ggz183

Fritz, H., Abdelsalam, M., Ali, K. A., Bingen, B., Collins, A. S., Fowler, A. R., et al. (2013). Orogen styles in the East African orogen: A review of the neoproterozoic to cambrian tectonic evolution. *Journal of African Earth Sciences*, *86*, 65–106. https://doi.org/10.1016/j.jafrearsci.2013.06.004

Fuchs, L., & Becker, T. W. (2019). Role of strain-dependent weakening memory on the style of mantle convection and plate boundary stability. *Geophysical Journal International*, *218*(1), 601–618. https://doi.org/10.1093/gji/ggz167

Gerya, T. V. (2019). *Introduction to numerical geodynamic modelling* (2nd ed.). Cambridge University Press. https://doi.org/10.1017/9781316534243

Gerya, T. V., & Meilick, F. I. (2011). Geodynamic regimes of subduction under an active margin: Effects of rheological weakening by fluids and melts. *Journal of Metamorphic Geology*, *29*(1), 7–31. https://doi.org/10.1111/j.1525-1314.2010.00904.x

Gleason, G. C., & Tullis, J. (1995). A flow law for dislocation creep of quartz aggregates determined with the molten salt cell. *Tectonophysics*, *247*(1–4), 1–23. https://doi.org/10.1016/0040-1951(95)00011-B

Glerum, A., Brune, S., Stamps, D. S., & Strecker, M. R. (2020). Victoria continental microplate dynamics controlled by the lithospheric strength distribution of the East African Rift. *Nature Communications*, *11*(1), 2881. https://doi.org/10.1038/s41467-020-16176-x

Glerum, A., Thieulot, C., Fraters, M., Blom, C., & Spakman, W. (2018). Nonlinear viscoplasticity in ASPECT: Benchmarking and applications to subduction. *Solid Earth*, *9*(2), 267–294. https://doi.org/10.5194/se-9-267-2018

Gouiza, M., & Naliboff, J. B. (2021). Rheological inheritance controls the formation of segmented rifted margins in cratonic lithosphere. *Nature Communications*, *12*(1), 4653. https://doi.org/10.1038/s41467-021-24945-5

Gueydan, F., & Précigout, J. (2014). Modes of continental rifting as a function of ductile strain localization in the lithospheric mantle. *Tectonophysics*, *612–613*, 18–25. https://doi.org/10.1016/j.tecto.2013.11.029

Gueydan, F., Précigout, J., & Montési, L. G. J. (2014). Strain weakening enables continental plate tectonics. *Tectonophysics*, *631*, 189–196. https://doi.org/10.1016/j.tecto.2014.02.005

Gün, E., Pysklywec, R. N., Topuz, G., Göğüş, O. H., & Heron, P. J. (2024). Syn-Drift plate tectonics. *Geophysical Research Letters*, *51*(2), e2023GL105452. https://doi.org/10.1029/2023GL105452

Hansen, C. D., & Johnson, C. R. (2005). *The visualization handbook*. Elsevier-Butterworth Heinemann.

Hasterok, D., & Chapman, D. S. (2011). Heat production and geotherms for the continental lithosphere. *Earth and Planetary Science Letters*, *307*(1), 59–70. https://doi.org/10.1016/j.epsl.2011.04.034

Heine, C., & Brune, S. (2014). Oblique rifting of the equatorial atlantic: Why there is no Saharan Atlantic Ocean. *Geology*, *42*(3), 211–214. https://doi.org/10.1130/G35082.1

Heister, T., Dannberg, J., Gassmöller, R., & Bangerth, W. (2017). High accuracy mantle convection simulation through modern numerical methods–II: Realistic models and problems. *Geophysical Journal International*, *210*(2), 833–851. https://doi.org/10.1093/gji/ggx195

Heron, P. J., Peace, A. L., McCaffrey, K. J. W., Sharif, A., Yu, A. J., & Pysklywec, R. N. (2023). Stranding continental crustal fragments during continent breakup: Mantle suture reactivation in the Nain Province of Eastern Canada. *Geology*, *51*(4), 362–365. https://doi.org/10.1130/G50734.1

Heron, P. J., Peace, A. L., McCaffrey, K. J. W., Welford, J. K., Wilson, R., Van Hunen, J., & Pysklywec, R. N. (2019). Segmentation of rifts through structural inheritance: Creation of the Davis Strait. *Tectonics*, *38*(7), 2411–2430. https://doi.org/10.1029/2019TC005578

Heron, P. J., Pysklywec, R. N., & Stephenson, R. (2016a). Identifying mantle lithosphere inheritance in controlling intraplate orogenesis. *Journal of Geophysical Research: Solid Earth*, *121*(9), 6966–6987. https://doi.org/10.1002/2016JB013460

Heron, P. J., Pysklywec, R. N., & Stephenson, R. (2016b). Lasting mantle scars lead to perennial plate tectonics. *Nature Communications*, *7*(1), 11834. https://doi.org/10.1038/ncomms11834

Hirth, G., & Kohlstedt, D. (2003). Rheology of the upper mantle and the mantle wedge: A view from the experimentalists. In J. Eiler (Ed.), *Geophysical monograph series* (Vol. 138, pp. 83–105). American Geophysical Union. https://doi.org/10.1029/138GM06

Huismans, R. S., & Beaumont, C. (2003). Symmetric and asymmetric lithospheric extension: Relative effects of frictional-plastic and viscous strain softening. *Journal of Geophysical Research*, *108*(B10), 2002JB002026. https://doi.org/10.1029/2002JB002026

Hurley, P. M., Rand, J. R., Pinson, W. H., Fairbairn, H. W., De Almeida, F. F. M., Melcher, G. C., et al. (1967). Test of continental drift by comparison of radiometric ages: A pre-drift reconstruction shows matching geologic age provinces in west Africa and northern Brazil. *Science*, *157*(3788), 495–500. https://doi.org/10.1126/science.157.3788.495

Karato, S. I., & Wu, P. (1993). Rheology of the upper mantle: A synthesis. *Science*, *260*(5109), 771–778. https://doi.org/10.1126/science.260.5109.771

Klein, E. L., & Moura, C. A. V. (2008). São Luís craton and Gurupi belt (Brazil): Possible links with the West African craton and surrounding Pan-African belts. *Geological Society, London, Special Publications*, *294*(1), 137–151. https://doi.org/10.1144/SP294.8

Klein, E. L., Moura, C. A. V., & Pinheiro, B. L. S. (2005). Paleoproterozoic crustal evolution of the São Luís craton, Brazil: Evidence from Zircon geochronology and Sm-Nd Isotopes. *Gondwana Research*, *8*(2), 177–186. https://doi.org/10.1016/S1342-937X(05)71116-3

Kolb, J. (2014). Structure of the palaeoproterozoic nagssugtoqidian orogen, south-east Greenland: Model for the tectonic evolution. *Precambrian Research*, *255*, 809–822. https://doi.org/10.1016/j.precamres.2013.12.015

Konopásek, J., Cavalcante, C., Fossen, H., & Janoušek, V. (2020). Adamastor – An ocean that never existed? *Earth-Science Reviews*, *205*, 103201. https://doi.org/10.1016/j.earscirev.2020.103201

Kronbichler, M., Heister, T., & Bangerth, W. (2012). High accuracy mantle convection simulation through modern numerical methods: High accuracy mantle convection simulation. *Geophysical Journal International*, *191*(1), 12–29. https://doi.org/10.1111/j.1365-246X.2012.05609.x

Li, Z. X., Bogdanova, S. V., Collins, A. S., Davidson, A., De Waele, B., Ernst, R. E., et al. (2008). Assembly, configuration, and break-up history of Rodinia: A synthesis. *Precambrian Research*, *160*(1–2), 179–210. https://doi.org/10.1016/j.precamres.2007.04.021

Manatschal, G., Lavier, L., & Chenin, P. (2015). The role of inheritance in structuring hyperextended rift systems: Some considerations based on observations and numerical modeling. *Gondwana Research*, *27*(1), 140–164. https://doi.org/10.1016/j.gr.2014.08.006

Mason, A. J., & Brewer, T. S. (2004). Mafic dyke remnants in the Lewisian complex of the outer hebrides, NW scotland: A geochemical record of continental break-up and re-assembly. *Precambrian Research*, *133*(1–2), 121–141. https://doi.org/10.1016/j.precamres.2004.04.001

McCaffrey, K. J. W., Grocott, J., Garde, A. A., & Hamilton, M. A. (2004). Attachment formation during partitioning of oblique convergence in the Ketilidian orogen, south Greenland. *Geological Society, London, Special Publications*, *227*(1), 231–248. https://doi.org/10.1144/GSL.SP.2004.227.01.12

McKenzie, D. (1978). Some remarks on the development of sedimentary basins. *Earth and Planetary Science Letters*, *40*(1), 25–32. https://doi.org/10.1016/0012-821X(78)90071-7

Mohanty, S. (2011). Palaeoproterozoic assembly of the napier complex, southern India and western Australia: Implications for the evolution of the cuddapah basin. *Gondwana Research*, *20*(2–3), 344–361. https://doi.org/10.1016/j.gr.2011.03.009

Murphy, J. B., Gutierrez-Alonso, G., Nance, R. D., Fernandez-Suarez, J., Keppie, J. D., Quesada, C., et al. (2006). Origin of the rheic ocean: Rifting along a neoproterozoic suture? *Geology*, *34*(5), 325. https://doi.org/10.1130/G22068.1

Myers, J. S. (1987). The East Greenland Nagssugtoqidian mobile belt compared with the Lewisian complex. *Geological Society, London, Special Publications*, *27*(1), 235–246. https://doi.org/10.1144/GSL.SP.1987.027.01.20

Naliboff, J. B., & Buiter, S. J. H. (2015). Rift reactivation and migration during multiphase extension. *Earth and Planetary Science Letters*, *421*, 58–67. https://doi.org/10.1016/j.epsl.2015.03.050

Naliboff, J. B., Buiter, S. J. H., Péron-Pinvidic, G., Osmundsen, P. T., & Tetreault, J. (2017). Complex fault interaction controls continental rifting. *Nature Communications*, *8*(1), 1179. https://doi.org/10.1038/s41467-017-00904-x

Neuharth, D., Brune, S., Glerum, A., Heine, C., & Welford, J. K. (2021). Formation of continental microplates through rift linkage: Numerical modeling and its application to the flemish cap and sao paulo plateau. *Geochemistry, Geophysics, Geosystems*, *22*(4), e2020GC009615. https://doi.org/10.1029/2020GC009615

Neuharth, D., Brune, S., Wrona, T., Glerum, A., Braun, J., & Yuan, X. (2022). Evolution of rift systems and their fault networks in response to surface processes. *Tectonics*, *41*(3), e2021TC007166. https://doi.org/10.1029/2021TC007166

NOAA National Centers for Environmental Information. (2022). ETOPO 2022 15 arc-second global Relief model [Dataset]. *NOAA National Centers for Environmental Information*. https://doi.org/10.25921/FD45-GT74

Park, G. (2022). A regional explanation for Laxfordian tectonic evolution and its implications for the Lewisian terrane model. *Scottish Journal of Geology*, *58*(1), sjg2021-020. https://doi.org/10.1144/sjg2021-020

Peace, A. L., McCaffrey, K., Imber, J., Van Hunen, J., Hobbs, R., & Wilson, R. (2018). The role of pre-existing structures during rifting, continental breakup and transform system development, offshore West Greenland. *Basin Research*, *30*(3), 373–394. https://doi.org/10.1111/bre.12257

Peace, A. L., Phethean, J. J. J., Franke, D., Foulger, G. R., Schiffer, C., Welford, J. K., et al. (2020). A review of Pangaea dispersal and Large Igneous Provinces – In search of a causative mechanism. *Earth-Science Reviews*, *206*, 102902. https://doi.org/10.1016/j.earscirev.2019.102902

Pedrosa-Soares, A. (2001). The Araçuaí-west-Congo orogen in Brazil: An overview of a confined orogen formed during gondwanaland assembly. *Precambrian Research*, *110*(1–4), 307–323. https://doi.org/10.1016/S0301-9268(01)00174-7

Petersen, K. D., & Schiffer, C. (2016). Wilson cycle passive margins: Control of orogenic inheritance on continental breakup. *Gondwana Research*, *39*, 131–144. https://doi.org/10.1016/j.gr.2016.06.012

Piqué, A., & Laville, E. (1996). The central Atlantic rifting: Reactivation of Palaeozoic structures? *Journal of Geodynamics*, *21*(3), 235–255. https://doi.org/10.1016/0264-3707(95)00022-4

Pons, M., Rodriguez Piceda, C., Sobolev, S. V., Scheck-Wenderoth, M., & Strecker, M. R. (2023). Localization of deformation in a non-collisional subduction orogen: The roles of dip geometry and plate strength on the evolution of the broken andean foreland, sierras pampeanas, Argentina. *Tectonics*, *42*(8), e2023TC007765. https://doi.org/10.1029/2023TC007765

Precigout, J., Gueydan, F., Gapais, D., Garrido, C. J., & Essaifi, A. (2007). Strain localisation in the subcontinental mantle — A ductile alternative to the brittle mantle. *Tectonophysics*, *445*(3–4), 318–336. https://doi.org/10.1016/j.tecto.2007.09.002

Pysklywec, R. N., Beaumont, C., & Fullsack, P. (2002). Lithospheric deformation during the early stages of continental collision: Numerical experiments and comparison with South Island, New Zealand. *Journal of Geophysical Research*, *107*(B7). https://doi.org/10.1029/2001JB000252

Reeves, C., & De Wit, M. (2000). Making ends meet in Gondwana: Retracing the transforms of the Indian ocean and reconnecting continental shear zones. *Terra Nova*, *12*(6), 272–280. https://doi.org/10.1046/j.1365-3121.2000.00309.x

Richter, M. J. E. A., Brune, S., Riedl, S., Glerum, A., Neuharth, D., & Strecker, M. R. (2021). Controls on asymmetric rift dynamics: Numerical modeling of strain localization and fault evolution in the Kenya rift. *Tectonics*, *40*(5), e2020TC006553. https://doi.org/10.1029/2020TC006553

Rossum, G. van, & Drake, F. L. (2010). *The Python language reference (Release 3.0.1 [Repr.])*. Python Software Foundation.

Ruh, J. B., Tokle, L., & Behr, W. M. (2022). Grain-size-evolution controls on lithospheric weakening during continental rifting. *Nature Geoscience*, *15*(7), 585–590. https://doi.org/10.1038/s41561-022-00964-9

Rybacki, E., Gottschalk, M., Wirth, R., & Dresen, G. (2006). Influence of water fugacity and activation volume on the flow properties of fine-grained anorthite aggregates. *Journal of Geophysical Research*, *111*(B3), 2005JB003663. https://doi.org/10.1029/2005JB003663

Salazar-Mora, C. A., Huismans, R. S., Fossen, H., & Egydio-Silva, M. (2018). The Wilson cycle and effects of tectonic structural inheritance on rifted passive margin formation. *Tectonics*, *37*(9), 3085–3101. https://doi.org/10.1029/2018TC004962

Salazar-Mora, C. A., & Sacek, V. (2023). Effects of tectonic quiescence between orogeny and rifting. *Tectonics*, *42*(2), e2022TC007492. https://doi.org/10.1029/2022TC007492

Samsu, A., Micklethwaite, S., Williams, J. N., Fagereng, Å., & Cruden, A. R. (2023). Structural inheritance in amagmatic rift basins: Manifestations and mechanisms for how pre-existing structures influence rift-related faults. *Earth-Science Reviews*, *246*, 104568. https://doi.org/10.1016/j.earscirev.2023.104568

Schellart, W. P., Chen, Z., Strak, V., Duarte, J. C., & Rosas, F. M. (2019). Pacific subduction control on Asian continental deformation including Tibetan extension and eastward extrusion tectonics. *Nature Communications*, *10*(1), 4480. https://doi.org/10.1038/s41467-019-12337-9

Schiffer, C., Doré, A. G., Foulger, G. R., Franke, D., Geoffroy, L., Gernigon, L., et al. (2020). Structural inheritance in the North Atlantic. *Earth-Science Reviews*, *206*, 102975. https://doi.org/10.1016/j.earscirev.2019.102975

Schiffer, C., Peace, A., Phethean, J., Gernigon, L., McCaffrey, K., Petersen, K. D., & Foulger, G. (2019). The Jan Mayen microplate complex and the Wilson cycle. *Geological Society*, *470*, 393–414. https://doi.org/10.1144/SP470.2

Schiffer, C., Stephenson, R. A., Petersen, K. D., Nielsen, S. B., Jacobsen, B. H., Balling, N., & Macdonald, D. I. M. (2015). A sub-crustal piercing point for North Atlantic reconstructions and tectonic implications. *Geology*, G37245. https://doi.org/10.1130/G37245.1

Schofield, D. I., Thomas, R. J., Goodenough, K. M., De Waele, B., Pitfield, P. E. J., Key, R. M., et al. (2010). Geological evolution of the antongil craton, NE Madagascar. *Precambrian Research*, *182*(3), 187–203. https://doi.org/10.1016/j.precamres.2010.07.006

Scott, D. J., & Machado, N. (1995). UPb geochronology of the northern Torngat orogen, labrador, Canada: A record of palaeoproterozoic magmatism and deformation. *Precambrian Research*, *70*(3–4), 169–190. https://doi.org/10.1016/0301-9268(94)00038-S

Skogseid, J., Planke, S., Faleide, J. I., Pedersen, T., Eldholm, O., & Neverdal, F. (2000). NE Atlantic continental rifting and volcanic margin formation. *Geological Society, London, Special Publications*, *167*(1), 295–326). https://doi.org/10.1144/gsl.sp.2000.167.01.12

St-Onge, M. R., Van Gool, J. A. M., Garde, A. A., & Scott, D. J. (2009). Correlation of archaean and palaeoproterozoic units between northeastern Canada and western Greenland: Constraining the pre-collisional upper plate accretionary history of the trans-hudson orogen. *Geological Society, London, Special Publications*, *318*(1), 193–235. https://doi.org/10.1144/SP318.7

Sutton, J., & Watson, J. (1950). The pre-Torridonian metamorphic history of the Loch Torridon and Scourie areas in the North-West Highlands, and its bearing on the chronological classification of the Lewisian. *Quarterly Journal of the Geological Society*, *106*(1–4), 241–307. https://doi.org/10.1144/GSL.JGS.1950.106.01-04.16

Tatsumi, Y. (1989). Migration of fluid phases and genesis of basalt magmas in subduction zones. *Journal of Geophysical Research*, *94*(B4), 4697–4707. https://doi.org/10.1029/JB094iB04p04697

Teixeira, W., Oliveira, E. P., & Marques, L. S. (2017). Nature and evolution of the archean crust of the São Francisco craton. In M. Heilbron, U. G. Cordani, & F. F. Alkmim (Eds.), *São Francisco Craton, eastern Brazil* (pp. 29–56). Springer International Publishing. https://doi.org/10.1007/978-3-319-01715-0_3

Tetreault, J. L., & Buiter, S. J. H. (2012). Geodynamic models of terrane accretion: Testing the fate of island arcs, oceanic plateaus, and continental fragments in subduction zones. *Journal of Geophysical Research*, *117*(B8), 2012JB009316. https://doi.org/10.1029/2012JB009316

Tetreault, J. L., & Buiter, S. J. H. (2014). Future accreted terranes: A compilation of island arcs, oceanic plateaus, submarine ridges, seamounts, and continental fragments. *Solid Earth*, *5*(2), 1243–1275. https://doi.org/10.5194/se-5-1243-2014

Thomas, W. A. (2019). Tectonic inheritance at multiple scales during more than two complete Wilson cycles recorded in eastern North America. *Geological Society*, *470*, 337–352. https://doi.org/10.1144/SP470.4

Tucker, R. D., Ashwal, L. D., & Torsvik, T. H. (2001). U–Pb geochronology of Seychelles granitoids: A Neoproterozoic continental arc fragment. *Earth and Planetary Science Letters*, *187*(1), 27–38. https://doi.org/10.1016/S0012-821X(01)00282-5

Van Wijk, J. W. (2005). Role of weak zone orientation in continental lithosphere extension. *Geophysical Research Letters*, *32*(2). https://doi.org/10.1029/2004gl022192

Vauchez, A., Barruol, G., & Tommasi, A. (1997). Why do continents break-up parallel to ancient orogenic belts? *Terra Nova*, *9*(2), 62–66. https://doi.org/10.1111/j.1365-3121.1997.tb00003.x

Vink, G. E. (1984). A hotspot model for Iceland and the Vøring Plateau. *Journal of Geophysical Research*, *89*(B12), 9949–9959. https://doi.org/10.1029/JB089iB12p09949

Vink, G. E., Morgan, W. J., & Zhao, W.-L. (1984). Preferential rifting of continents: A source of displaced terranes. *Journal of Geophysical Research*, *89*(B12), 10072–10076. https://doi.org/10.1029/JB089iB12p10072

Wardle, R. J., James, D. T., Scott, D. J., & Hall, J. (2002). The southeastern Churchill province: Synthesis of a paleoproterozoic transpressional orogen. *Canadian Journal of Earth Sciences*, *39*(5), 639–663. https://doi.org/10.1139/e02-004

Wardle, R. J., Ryan, B., & Ermanovics, I. (1990). The eastern Churchill province, Torngat and new Québec orogens: An overview. *Geoscience Canada*, *17*(4).

Wheeler, J., Park, R. G., Rollinson, H. R., & Beach, A. (2010). The Lewisian complex: Insights into deep crustal evolution. *Geological Society, London, Special Publications*, *335*(1), 51–79. https://doi.org/10.1144/SP335.4

Willingshofer, E., Sokoutis, D., Luth, S. W., Beekman, F., & Cloetingh, S. (2013). Subduction and deformation of the continental lithosphere in response to plate and crust-mantle coupling. *Geology*, *41*(12), 1239–1242. https://doi.org/10.1130/G34815.1

Wilson, J. T. (1966). Did the Atlantic close and then Re-open? *Nature*, *211*(5050), 676–681. https://doi.org/10.1038/211676a0

Wilson, J. T. (1969). Static or mobile earth: The current scientific revolution. *Tectonophysics*, *7*(5–6), 600–601. https://doi.org/10.1016/0040-1951(69)90033-X

Xue, L., Moucha, R., Kolawole, F., Muirhead, J. D., & Scholz, C. A. (2024). The influence of the strength of pre-existing weak zones on rift geometry and strain localization. *Tectonophysics*, *890*, 230472. https://doi.org/10.1016/j.tecto.2024.230472

Yu, A. J. (2025). A recipe for exotic continental fragment formation: Key constraints from numerical rift models [Dataset]. *Zenodo*. https://doi.org/10.5281/ZENODO.14847235